



# Changing chemistry of particulate manganese in the near- and far-field hydrothermal plumes from 15°S East Pacific Rise and its influence on metal scavenging

Jong-Mi Lee<sup>a,\*</sup>, Phoebe J. Lam<sup>a,\*</sup>, Sebastian M. Vivancos<sup>b,c</sup>, Frank J. Pavia<sup>b,c,d</sup>, Robert F. Anderson<sup>b,c</sup>, Yanbin Lu<sup>e,f</sup>, Hai Cheng<sup>e,g</sup>, Pu Zhang<sup>e,g</sup>, R. Lawrence Edwards<sup>e</sup>, Yang Xiang<sup>a</sup>, Samuel M. Webb<sup>h</sup>

<sup>a</sup> Ocean Sciences Department, University of California, Santa Cruz, Santa Cruz, CA 95064, USA

<sup>b</sup> Lamont-Doherty Earth Observatory of Columbia University, Palisades, NY 10964, USA

<sup>c</sup> Department of Earth and Environmental Sciences, Columbia University, New York, NY 10027, USA

<sup>d</sup> Division of Geological and Planetary Sciences, California Institute of Technology, Pasadena, CA 91125, USA

<sup>e</sup> Department of Earth and Environmental Sciences, University of Minnesota, Minneapolis, MN 55455, USA

<sup>f</sup> Earth Observatory of Singapore, Nanyang Technological University, Singapore 639798, Singapore

<sup>g</sup> Institute of Global Environmental Change, Xi'an Jiaotong University, Xi'an 710054, China

<sup>h</sup> Stanford Synchrotron Radiation Lightsource, Stanford University, Menlo Park, CA 94025, USA

Received 26 August 2020; accepted in revised form 13 February 2021; Available online 22 February 2021

## Abstract

Dissolved Mn(II) in the hydrothermal plume is known to be microbially oxidized to form Mn(III/IV) oxides, and the Mn oxides scavenge other trace elements in seawater.

In the GEOTRACES GP16 cruise, dissolved Mn (dMn) and particulate Mn (pMn) were found to be transported over 4000 km westwards from the Southern Eastern Pacific Rise. Previous studies in this plume showed different removal rates of dMn and pMn as well as pMn size distribution between the near-field (<80 km from the ridge axis) and far-field (>80 km) plumes. In order to understand Mn cycling in these plumes, spatial distribution, oxidation states, and mineral structures of Mn in small size fraction (SSF; 0.8–51 μm) and large size fraction (LSF; >51 μm) particles from the near-field and far-field plumes were examined using micro X-ray fluorescence spectrometry (μ-XRF), X-ray absorption near-edge structure spectroscopy (XANES), chemical species mapping, and extended X-ray absorption fine-structure spectroscopy (EXAFS). In the near-field plume, pMn in the SSF is dominated by oxidized Mn with Mn(III) fractions of ~30%. They are a mixture of δ-MnO<sub>2</sub> and triclinic birnessites that is known to be formed as a result of autocatalytic Mn(II) oxidation at the surface of freshly-formed δ-MnO<sub>2</sub>, suggesting that both microbial and autocatalytic Mn oxidation occur in the near-field plume. The LSF pMn in the near-field plume is also oxidized and often found in large aggregates several hundreds of μm in size. These aggregates settle out in the near-field and during transport, and are not found in the far-field plume. In the far-field plume where Mn oxides are not newly formed, pMn in the SSF is oxidized, but their Mn(III) fractions are smaller than in the near-field pMn. Unlike the SSF, the far-field plume LSF pMn is dominated by reduced Mn, implying very slow aggregation of pMn in the far-field plume. The different characteristics of pMn between the near-field and far-field plumes affect its scavenging of other trace elements. In the near-field plume, Co, Mo, <sup>231</sup>Pa are associated with pMn, but not in the far-field plume. <sup>231</sup>Pa is adsorbed to pFe rather than pMn in the far-field plume, and Pb is adsorbed to pFe in the entire plume. The result shows that freshly-formed Mn oxides in the near-field plume have higher scavenging capacity than the far-field plume pMn.

\* Corresponding authors.

E-mail addresses: [jm\\_lee@ucsc.edu](mailto:jm_lee@ucsc.edu) (J.-M. Lee), [pjlam@ucsc.edu](mailto:pjlam@ucsc.edu) (P.J. Lam).

Our findings suggest that the mineralogical age of Mn oxides may be an important parameter that controls the scavenging of many other trace elements and isotopes.

© 2021 The Author(s). Published by Elsevier Ltd. This is an open access article under the CC BY-NC-ND license (<http://creativecommons.org/licenses/by-nc-nd/4.0/>).

**Keywords:** Manganese; Particle chemistry; Hydrothermal plume particles; Scavenging; Micro X-ray fluorescence ( $\mu$ -XRF) spectrometry; X-ray absorption near edge structure (XANES) spectroscopy; X-ray microprobe chemical speciation mapping; Extended X-ray absorption fine-structure (EXAFS) spectroscopy; East Pacific Rise; GEOTRACES GP16; Eastern Pacific Zonal Transect

## 1. INTRODUCTION

Redox cycling of manganese (Mn) plays an important role in ocean biogeochemistry. Its reduced form, Mn(II), is soluble and is taken up by phytoplankton to be used in photosynthesis and other biological processes (Raven, 1990; Peers and Price, 2004). On the other hand, oxidized Mn forms Mn(III/IV) oxide minerals that can effectively scavenge and remove other trace metals in seawater due to their high sorptive and oxidative capacity (see review by Tebo et al., 2004). Oxidation of Mn occurs through two-step electron transfers (Luther, 2005). At seawater pH, the oxidation of Mn(II) to Mn(IV) by  $O_2$  is limited despite being thermodynamically favorable because of the reactivity barrier imposed by the first electron transfer step (Luther, 2010; Hansel and Learman, 2015). Manganese oxidation can occur via catalyzation by mineral surfaces or microbial mediation, yet the former is orders of magnitude slower than the latter (Nealson et al., 1988; Tebo, 1991; Junta and Hochella, 1994). Thus, Mn oxidation in nature is thought to be largely microbially mediated, although its pathways and mechanisms are not fully defined yet. Laboratory studies using Mn-oxidizing bacteria and fungi have shown that Mn(II) is directly oxidized enzymatically on the outermost layer of their cells or spores (Nealson and Ford, 1980; vanWaasbergen et al., 1996; Francis and Tebo, 2002; Miyata et al., 2004; Dick et al., 2008; Butterfield et al., 2013). Recently, more Mn oxidation pathways have been identified including indirect oxidation via extracellular superoxide ( $O_2^-$ ) released from bacteria or fungi (Learman et al., 2011a; Hansel et al., 2012; Tang et al., 2013) and autocatalytic oxidation of Mn(II) at the surface of microbially-formed Mn(III/IV) oxides (Bargar et al., 2005a; Learman et al., 2011b). The microbial Mn oxidation primarily precipitates layers of poorly crystalline Mn(IV) oxides with hexagonal symmetry that is similar in structure to  $\delta$ -MnO<sub>2</sub> (Bargar et al., 2000; Villalobos et al., 2003), but further reactions with dissolved Mn(II) and/or other cations can yield various secondary products, such as 10-Å Na phyllo-manganate, feitknechtite, hausmannite, manganite, todorokite, and triclinic birnessite (Mandernack et al., 1995; Bargar et al., 2005a; Feng et al., 2010; Learman et al., 2011b; Yang et al., 2019).

At hydrothermal vents, reducing hydrothermal fluids enriched in Mn(II) are injected to the ocean (Edmond et al., 1982). Mixing of these vent fluids with more oxidizing ambient seawater allows oxidation of Mn(II) in the plume. The removal of Mn(II) by microbially-mediated oxidation is supported by several observations, such as decreased Mn(II) removal by poisons like sodium azide (Cowen

et al., 1986; Cowen et al., 1990; Mandernack and Tebo, 1993; Dick et al., 2009), isolation of Mn-oxidizing bacteria from vent sites (Ehrlich, 1983; Dick et al., 2006), and observation of Mn-coated bacteria in the vent plume by transmission electron microscopy (TEM) (Cowen et al., 1986; Campbell et al., 1988; Cowen et al., 1998). The Mn particles in the Guaymas Basin hydrothermal plume have been also shown to be hexagonal birnessite or  $\delta$ -MnO<sub>2</sub>-like mineral that is similar to the product of microbial Mn oxidation (Dick et al., 2009). Once the hydrothermal Mn is converted to Mn oxides, they eventually settle and sink to the seafloor, scavenging other trace elements (German and Seyfried Jr., 2014 and references therein), and contributing to the deposition of metalliferous sediments. Despite these removal processes, however, dissolved Mn from hydrothermal sources has been observed thousands of kilometers away from the ridge axis (Klinkhammer, 1980; Klinkhammer and Hudson, 1986), and Mn-rich metalliferous sediments have been also found on a similar spatial scale (Bostrom and Peterson, 1966, 1969). These observations imply that the hydrothermal Mn is removed from the plume in a time scale comparable to the basin-scale dispersion. However, previous studies on the cycling of hydrothermal Mn have been focused on the processes close (within  $\sim$ 20 km) to the sources (Campbell et al., 1988; Cowen et al., 1990; Mandernack and Tebo, 1993), and little is known about the reactions occurring in the distal plume.

The cycling of Mn in the non-buoyant hydrothermal plume is often compared to that of Fe because soluble Fe(II) is also enriched in hydrothermal fluids and is removed by oxidation to Fe(III) oxyhydroxides (von Damm, 1990; Feely et al., 1996; German and Seyfried Jr., 2014), although its oxidation process is abiotic and several orders of magnitude faster than that of Mn (Field and Sherrell, 2000). The recent GEOTRACES GP16 cruise to the Eastern South Pacific collected hydrothermal plume samples from the 15°S East Pacific Rise along  $\sim$ 4500 km of the plume transport path. Studies from this cruise showed that hydrothermally derived Fe and Mn can travel over 4000 km in both dissolved and particulate (materials collected by 0.45  $\mu$ m or 0.8  $\mu$ m filtration) phases (Resing et al., 2015; Fitzsimmons et al., 2017; Lee et al., 2018). In these studies, different behaviors of Fe and Mn have been observed between near-field (<87 km) and far-field plumes (>87 km). First of all, dissolved Fe (dFe) and Mn (dMn) are removed only in the near-field plumes but remain conservative in the rest of the plume (Resing et al., 2015). Both particulate Fe (pFe) and Mn (pMn) are also removed rapidly in the near-field plume, but in the far-field plume, pMn is removed more slowly than pFe (Fitzsimmons

et al., 2017; Lee et al., 2018). Lastly, the size partitioning of pMn in the near-field plume is unusual, with ~50% in large (>51  $\mu\text{m}$ ) particles, whereas pFe and other elements have only ~20% of the particle phase in large particles. This difference in size distribution disappears in the far-field plume where all elements including Mn mainly (70–80%) consist of small (0.8–51  $\mu\text{m}$ ) particles (Lee et al., 2018). These observations hint that different processes govern the cycling of Fe and Mn in the near-field and far-field plumes. Further studies revealed the physicochemical forms of dFe and pFe and their transformation along the plume (Fitzsimmons et al., 2017; Hoffman et al., 2018), but not much attention has been paid to Mn in these plumes.

In this study, we present the chemistry of Mn in small (0.8–51  $\mu\text{m}$ ) and large (>51  $\mu\text{m}$ ) hydrothermal plume particles collected at two near-field and two far-field stations from the GP16 cruise. Spatial distribution, oxidation states, and mineral structures of Mn in these particles were examined using micro X-ray fluorescence spectrometry ( $\mu\text{-XRF}$ ), X-ray absorption near-edge structure spectroscopy (XANES) and chemical species mapping, and extended X-ray absorption fine-structure spectroscopy (EXAFS), respectively. Details of each analytical technique are reviewed in Lam et al. (2015b). Based on the results of this study and the distributions of dMn, pMn, and particle size in the plume known from the previous studies, we discuss the cycling of Mn in the near-field and far-field plumes and its implication on the scavenging of other trace elements.

## 2. METHODS

### 2.1. Sampling location

Hydrothermal plume particles were collected during the U.S. GEOTRACES East Pacific Zonal Transect (EPZT) cruise (GP16 section) (October–December 2013), which sailed from Manta, Ecuador to Tahiti (Fig. 1). The cruise crossed over the 15°S Southern East Pacific Rise (SEPR) ridge axis at station 18, and the rest of the stations are located downstream of the non-buoyant plume spreading from the SEPR to the west. Hydrothermal activities along the SEPR have been previously well documented by mantle-derived, high  $^3\text{He}$  ( $^3\text{He}_{\text{xs}}$ ) (Lupton and Craig, 1981; Feely et al., 1996). In the GP16 cruise, the hydrothermal plume was identified by anomalously high  $^3\text{He}_{\text{xs}}$  at depths between 2200 m and 3000 m (Jenkins et al., 2018),

as well as high dFe and dMn concentrations (Resing et al., 2015). Based on the linear correlations between  $^3\text{He}_{\text{xs}}$  and dFe and dMn, Resing et al. (2015) suggested that the plume detected at station 20 to the westernmost station is a continuous plume and mainly a mixture of hydrothermal materials derived from vents located further south (17–18.5°S), which was carried north and then west by topographically-steered currents (Shimmield and Price, 1988; Hautala and Riser, 1993; Talley and Johnson, 1994). On the other hand, the plume with relatively low  $^3\text{He}_{\text{xs}}$  at station 18 was attributed to a local hydrothermal source (Jenkins et al., 2018). In this study, we investigated hydrothermal plume particles from station 18 over the ridge axis, and from stations 20, 21, and 25 that are approximately 81 km, 243 km, and 1350 km off from the ridge axis, respectively. Station 23 was not chosen because it is thought to be a circulation feature and falls off from the continuous westward aging pattern of the plume (Jenkins et al., 2018). As described earlier, stations 18 and 20 show different removal patterns of dMn and pMn and size distribution of pMn from the rest of the stations. Therefore, we will refer to stations 18 and 20 as “near-field stations” and stations 21 and 25 as “far-field stations”.

### 2.2. Sample collection

Particle samples were collected using battery-powered in-situ pumps (McLane WTS-LV) that were set up with two mini-MULVFS filter holders (Bishop et al., 2012). The seawater entering each filter holder first passes through 142 mm diameter, 51  $\mu\text{m}$  pore-size polyester pre-filter followed by a pair of quartz fiber Whatman QMA filters (“QMA” side) or a pair of 0.8  $\mu\text{m}$  pore-size polyethersulfone Supor™ filters (“Supor” side). After collection, filters were cut into 1/16 or 1/8 wedges with a ceramic rotary-blade, and then dried on acid-leached polystyrene “egg-grate” grids in a laminar flow bench (HEPA filter). The dried samples were stored in particle-free cleanroom polyethylene bags (KNF Flexpak). Further details of the pump operation and particle collection for the entire cruise are described in Heller et al. (2017). All filters were pre-cleaned with trace-metal grade HCl before the cruise and on-board filter processing was performed within a HEPA-filtered bubble. The small and large size fraction (SSF and LSF) particles used for X-ray fluorescence spectroscopy are from the top layer of the Supor-side Supor filters (st, 0.8–51  $\mu\text{m}$ ) and the QMA-side pre-filters (qp,

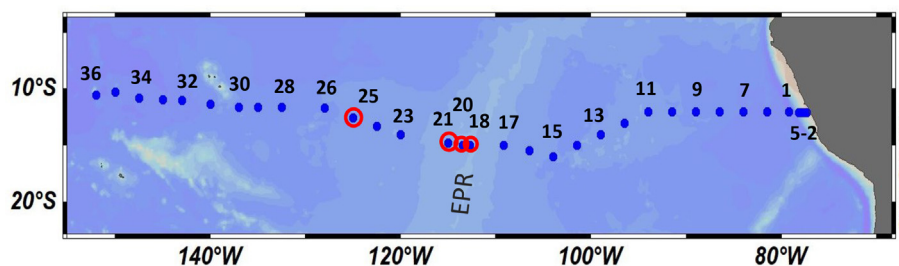


Fig. 1. Sampling locations of the GP16 EPZT cruise. The particle samples used in this study are from the circled stations.

>51  $\mu\text{m}$ ), respectively. From another subset of the same filters, trace element concentrations were measured. The analytical methods and results of the elemental concentrations were published in Lee et al. (2018). The elemental concentrations data were considered when interpreting the results of X-ray fluorescence spectroscopy.

### 2.3. X-ray absorption spectroscopy

#### 2.3.1. Photodamage of samples and selection of beamlines

As a preliminary study, we collected micro (beam size:  $4 \times 4 \mu\text{m}^2$ ) XRF ( $\mu$ -XRF) and quick Mn XANES ( $\mu$ -QXANES) data from the samples at the Berkeley Advanced Light Source (ALS) beamline 10.3.2. Collecting Mn X-ray fluorescence data from the marine particles was challenging because of heterogeneity and low Mn concentrations of the samples (0.1–18.6 nmol Mn/cm<sup>2</sup> of filter). In particular, photoreduction and photoablation seemed to occur occasionally when a particle was irradiated with a high, focused flux of X-rays for too long at room temperature. For instance, photodamage was observed after a sample was irradiated for  $\sim 100$  seconds with  $\sim 10^9$  ph/s of energy, and it occurred more frequently when the particles had high organic contents.

Partly in response to these problems, bulk XANES and EXAFS of SSF particles were acquired at the Stanford Synchrotron Radiation Lightsource (SSRL) beamline 11-2. At this beamline, the samples were loaded within a liquid nitrogen cryostat to minimize any photo-reaction during the data collection, which was confirmed by no change in the X-ray fluorescence spectra during >20 scans. The large beam size ( $10 \times 1 \text{mm}^2$ ) of this beamline allowed for the collection of integrated signals from heterogeneous particles. The SSF particle samples were analyzed on the Supor filters on which they were collected. In order to increase the amount of sample materials irradiated by the beam, a 1/16 or 1/8 slice of the Supor filters (equivalent to 25–50 liters filtered) was folded so that 20–60 layers were fit into a sample holder. Because Supor filters have negligible Mn, the detected fluorescence spectra were the integration of those from all particles lying on the pathway of  $10 \times 1 \text{mm}^2$  beam penetrating through 20–60 filter layers.

For LSF particles, bulk measurement could not be performed because the particles are distributed sparsely on a polyethylene prefilter that contains relatively high Mn. Thus, the Mn oxidation state of the LSF particles was measured using micro ( $5 \times 5 \mu\text{m}^2$ ) chemical mapping techniques at SSRL beamline 2-3, which has a lower photon flux at the Mn K-edge than the ALS beamline 10.3.2. Since beamline 2-3 was not equipped with cryogenic sample cooling system, potential photodamage was monitored during the measurement. The photodamage was not observable during chemical mapping because each  $5 \times 5 \mu\text{m}^2$  area of the samples was exposed to X-rays for less than a second during the entire procedure (see Section 2.3.3). EXAFS spectra of the LSF samples could not be obtained at this beamline, however, because it required the samples to be irradiated for >12 hours at their concentration range, which will likely cause photodamage. Only one EXAFS spectra was collected from a LSF particle. This was done at SSRL

beamline 10-2, which has a larger beam size ( $10 \times 10 \mu\text{m}^2$ ) and thus lower photon flux/area than SSRL beamline 2-3, to reduce photodamage.

#### 2.3.2. Bulk XANES and EXAFS for SSF particles

Averaged oxidation states of Mn in SSF (0.8–51  $\mu\text{m}$ ) particles were determined by bulk Mn XANES at SSRL beamline 11-2 except for four samples whose Mn concentrations were too low for XANES analysis (Supp. Table 1). For these low-Mn samples, the Mn oxidation state was measured using Mn chemical species mapping at SSRL 2-3 (Section 2.3.3). At SSRL 11-2, the Mn K-edge XANES spectra were collected using a Si (2 2 0) monochromator ( $\Phi = 90^\circ$ ) to create a monochromatic beam with a  $10 \times 1 \text{mm}^2$  beam size. The monochromator was calibrated using a potassium permanganate (KMnO<sub>4</sub>) XANES scan with its pre-edge set to 6543.34 eV. Fluorescence spectra were collected from  $-200$  to approximately  $+450$  eV around the Mn K-edge (6539 eV), using a Canberra 100-pixel Ge solid-state monolith detector cooled with liquid nitrogen. Among the SSF samples studied by XANES, three near-field samples (GT8437st, GT8705st, and GT8436st) were further examined by EXAFS to elucidate the mineral structure of Mn in the particles. The EXAFS spectra could not be taken from far-field SSF samples due to their low Mn contents (<1.4 nmol Mn/cm<sup>2</sup> of filter). The instrumental setting for the EXAFS analysis was the same as for the XANES, but for EXAFS, the fluorescence spectra were collected to approximately  $+600$  eV above the Mn K-edge, which is equivalent to  $k = \sim 11.5 \text{\AA}^{-1}$ . The spectra beyond  $k = 12 \text{\AA}^{-1}$  were not collected due to the interference of high fluorescence from Fe in the samples.

The collected XANES and EXAFS spectra were averaged, background-subtracted, normalized, and deglitched as necessary, and least squares fitting was performed using the SIXPACK software program (Webb, 2005). The proportions of Mn(II), Mn(III), and Mn(IV) in XANES spectra were estimated by conducting linear combination fitting with the three model Mn compounds, pyroxmangite (Mn<sup>II</sup>-SiO<sub>3</sub>), feitknechtite (Mn<sup>III</sup>OOH), and  $\delta$ -Mn<sup>IV</sup>O<sub>2</sub>, respectively (See Section 2.3.4 for the choice of the model compounds) (Fig. 2). Then, the average Mn oxidation state of the sample was calculated from the Mn(II), Mn(III), and Mn(IV) proportions. Determination of Mn oxidation state based on XANES spectra fitting is well established (Bargar et al., 2005a; Webb et al., 2005a; Manceau et al., 2012), and the errors of this method have been previously assessed by Bargar et al. (2005a) with  $1\sigma$  errors of Mn(II), Mn(III), and Mn(IV) fractions to be 1.7%, 2.6%, and 2.9%, respectively, and  $\pm 0.02$  for Mn oxidation state. We have estimated the Mn oxidation states of reference Mn XANES spectra (Manceau et al., 2012, 2014) in the same way as our samples, and the result agreed well with the reported values (Supp. Fig. 1). For EXAFS, the  $\chi(k)$  spectra were  $k^3$ -weighted and the data in a  $k$  range of 3–11.3  $\text{\AA}^{-1}$  was used for linear combination fitting. The reference EXAFS spectra used for fitting included those of  $\delta$ -MnO<sub>2</sub>, hexagonal Na-birnessite (Mn<sup>IV</sup>O<sub>2</sub>), triclinic Na-birnessite (Mn<sup>III</sup>,<sup>IV</sup>O<sub>2</sub>), groutite ( $\alpha$ -Mn<sup>III</sup>OOH), feitknechtite ( $\beta$ -Mn<sup>III</sup>OOH), hausmannite (Mn<sup>II</sup>Mn<sup>III</sup>O<sub>4</sub>), synthetic

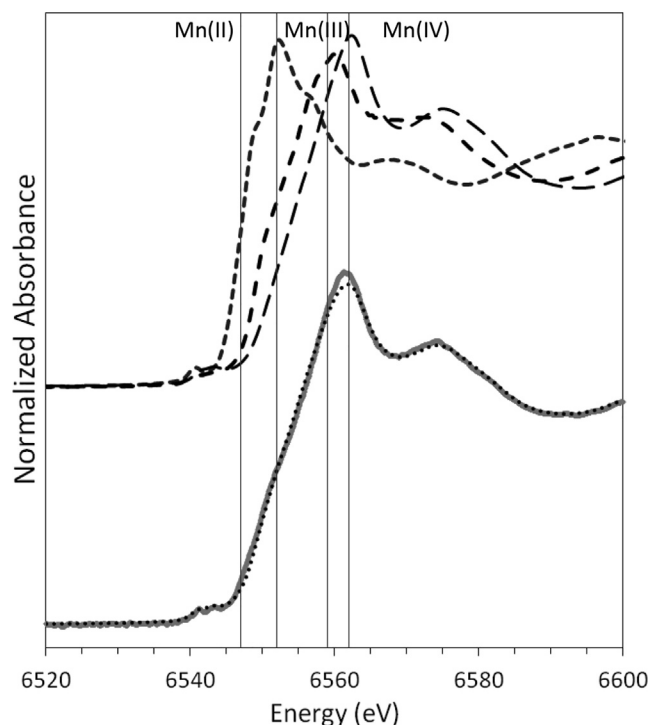


Fig. 2. Mn K-edge bulk XANES spectra of the SSF particles from station 20, 2550 m depth (GT8705st) (grey line) and the fit with 5% Mn(II), 29% Mn(III), and 66% Mn(IV) (dotted line), which yields a Mn oxidation state of 3.61. The three XANES spectra on top represent the model spectra for Mn(II) (pyroxmangite), Mn(III) (feitknechtite), and Mn(IV) ( $\delta$ -MnO<sub>2</sub>). The four vertical lines indicate the incident energies used to generate the Mn chemmap – 6547.0, 6552.0, 6559.0, and 6562.0 eV.

todorokite ((Na,Ca,K)(Mg,Mn<sup>II</sup>)Mn<sup>IV</sup>O<sub>14</sub>·5H<sub>2</sub>O), pyrolusite ( $\beta$ -Mn<sup>IV</sup>O<sub>2</sub>), pyroxmangite (Mn<sup>II</sup>SiO<sub>3</sub>), hureaulite (Mn<sup>II</sup>(PO<sub>3</sub>OH)<sub>2</sub>(PO<sub>4</sub>)<sub>2</sub>·4H<sub>2</sub>O), lithiophorite ((Al,Li)Mn<sup>III,IV</sup>O<sub>2</sub>(OH)<sub>2</sub>), rhodochrosite (Mn<sup>II</sup>CO<sub>3</sub>), Mn(II)-sorbed POC, Mn(II)-sorbed PIC, Mn-sorbed ferrihydrite, and Mn<sup>II</sup>S. The fitting was performed using various combinations of the reference spectra until the best fit was established by minimization of the R-factor (Newville, 2001).

### 2.3.3. Micro XRF ( $\mu$ -XRF) and manganese chemical species mapping for LSF particles

Spatial distribution of Mn in individual LSF particles and their oxidation states were examined by  $\mu$ -XRF and microprobe chemical speciation map (“chemmap”) analysis at beamline 2-3 at the SSRL. As at SSRL beamline 11-2, the Si (2 2 0) monochromator ( $\Phi = 90^\circ$ ) was calibrated using KMnO<sub>4</sub> (pre-edge at 6543.34 eV). The general procedure for mapping LSF particles was as follows. First, a randomly chosen area of the filter was mapped with incident energy of 7300 eV, a beam size of 10  $\times$  10  $\mu$ m<sup>2</sup>, and a dwell time of 20 ms, to locate Mn-bearing particles on the filter. The surveyed area was approximately 2400  $\times$  1600  $\mu$ m<sup>2</sup> for near-field samples and about three times greater for far-field samples where particle loads were low. From this “coarse” map, smaller areas around Mn-bearing particles were chosen and further mapped at 7300 eV to measure the distribution of multiple elements (Mn, Fe, Cr, Ti, Ca, K, Cl, S, P, V, and Si) ( $\mu$ -XRF), and at four energies around the Mn K-edge (6547.0, 6552.0, 6559.0, and 6562.0 eV) to determine the spatial distribution of Mn ox-

idation states in the particles. The fluorescence data from these “fine” maps were collected with a 5  $\times$  5  $\mu$ m<sup>2</sup> beam size and a 50 ms dwell time.

The four XRF maps collected around the Mn K-edge were deadtime corrected, registered, and compiled into a single file that will be referred to as a “chemmap” or “speciation map”. The Mn fluorescence originating from the polyester filter material was corrected using Ti that is also enriched in the polyethylene prefilter, similar to a procedure used by Lam et al. (2006), but adapted for chemical species mapping. The Mn:Ti ratio of an empty prefilter was obtained at each incident energy. Then, in each energy map, the Mn from the prefilter was subtracted based on the measured Ti fluorescence and the Mn:Ti ratio of the filter at the corresponding energy. The Ti contents are negligibly low in the studied LSF particles (Lee et al., 2018), so the measured Ti is dominated by the Ti in the filter. After correction for the filter Mn, the proportions of Mn(II), Mn(III), and Mn(IV) for each pixel of the map were calculated using SMAK software (Webb, 2011). Then, the Mn(II), Mn(III), and Mn(IV) contributions were summed for an entire particle area to yield an average Mn oxidation state of the particle. Depending on the abundance of Mn-bearing particles on the filter, 5–22 particles were examined in each sample (Supp. Table 2) except two samples from station 25 where <5 particles were studied. The Mn oxidation states of the individual particles were weighted by the particle’s Mn contents to yield an average Mn oxidation state of the sample.

### 2.3.4. Development of Mn chemical species mapping for hydrothermal plume samples

Chemical speciation or multi-energy mapping methods have been previously developed and applied to determine oxidation state of Mn in Mn-oxidizing fungus (Hansel et al., 2012) and Mn deposits in drill cores (Johnson et al., 2013). The choice of appropriate incident energies and model compounds used for chemical species mapping can vary between different sample types and environmental settings. As this approach had not been applied to hydrothermal plume samples before, we first undertook a survey of Mn minerals present in the samples. Three SSF and three LSF samples from the near-field and far-field plumes were mapped for Mn at Berkeley ALS beamline 10.3.2. ( $I_0 = 7010$  eV,  $4 \times 4 \mu\text{m}^2$  spot size, dwell time = 50 ms), and quick  $\mu$ -XANES ( $\mu$ -QXANES) were collected from 41 Mn hotspots. The resulting spectra were deadtime corrected, energy-calibrated, pre-edge subtracted and post-edge normalized using the software available from the beamline website (<https://als.lbl.gov/beamlines/10-3-2/>). Each sample spectrum was then fitted with various ( $n = 28$ ) reference Mn mineral spectra available at the beamline library (Manceau et al., 2012, 2014) using linear combination fitting. Several minerals repeatedly appeared as major components of the Mn present in the hydrothermal plume samples: pyroxmangite ( $\text{MnSiO}_3$ ), feitknechtite ( $\beta$ - $\text{MnOOH}$ ), and  $\delta$ - $\text{MnO}_2$ . Thus, we chose these minerals as model compounds for Mn(II), Mn(III), and Mn(IV) bearing minerals in our samples, respectively. Indeed, later PCA analysis of sample (micro and bulk) Mn XANES spectra confirmed that the Mn in most samples, with the exception of a few samples with reduced Mn that appeared to have an unidentifiable component, can be modeled with these three compounds (Supp. Fig. 2). Using the “chemmap error estimator calculator” program at the beamline (see Nicholas et al. (2017) for mathematical basis of chemmap error estimator software), four energies were chosen (6546.0, 6551.0, 6558.0, and 6561.0 eV) that were best able to distinguish between the three model spectra. At the ALS beamline 10.3.2, the monochromator was calibrated so that the first inflection point of the Mn foil XANES scan is set at 6537.67 eV. At the SSRL beamline 2-3, the same feature of the Mn foil XANES appeared 1.0 eV higher than at ALS 10.3.2 due to the different monochromator calibration methods of the two facilities. Thus, at SSRL 2-3, incident energies of 6547.0, 6552.0, 6559.0, and 6562.0 eV were used to generate chemmaps (Fig. 2).

The reliability of the Mn chemical mapping technique to estimate average oxidation state was assessed in three ways. First, reference Mn XANES spectra in the library were treated as unknowns, and we estimated their average oxidation states by sampling the reference spectra at the four energies used for our chemmap procedure and compared against the average oxidation states determined by Manceau et al. (2012, 2014) using XANES. These reference XANES spectra include those from both pure-valence Mn minerals and mixed-valence Mn minerals. The Mn average oxidation states that resulted from the chemmap calculation agreed well with the known values, falling on the 1:1 line (Fig. 3a).

Secondly, at SSRL beamline 2-3, dozens of  $\mu$ -XANES spectra ( $n = 48$ ) were taken from random Mn-rich spots after samples were analyzed for Mn chemmap. The Mn oxidation states of the spots were calculated from the  $\mu$ -XANES spectra in the same way that bulk XANES spectra were processed (Section 2.3.1), and the result was compared to that computed from chemmap for the corresponding spots. The Mn oxidation state calculated from chemmap generally agrees with that from  $\mu$ -XANES, but the former tends to be  $\sim 14\%$  higher than the latter (Fig. 3b). For these samples, the chemical species mapping seems to underestimate the fractions of Mn(III) and instead overestimates fractions of Mn(IV), whereas it estimates the fractions of Mn(II) relatively well (Supp. Fig. 3). This disagreement may indicate that the energies chosen for chemical mapping cannot distinguish Mn(III) and Mn(IV) in the samples effectively. Alternatively, the samples may have been photo-reduced during  $\mu$ -XANES collection because they were irradiated by X-ray at room temperature for a longer time for  $\mu$ -XANES ( $\sim 9$  min for  $5 \times 5 \mu\text{m}^2$  area) than for chemmap ( $< 1$  min for the same area). Because  $\mu$ -XANES were obtained after chemical mapping, the photoreduction of the sample could make the  $\mu$ -XANES-determined oxidation states appear lower than the chemmap-determined values. If the offset between chemmap and  $\mu$ -XANES is due to inadequate choice of energies used for chemmap, the chemmap-determined oxidation states could be corrected downward using an empirical fit. If the offset is due to photoreduction during the collection of  $\mu$ -XANES, then the chemmap-determined oxidation state should be more accurate.

Lastly, a sufficiently large area ( $1800 \times 400 \mu\text{m}^2$ ) of an SSF sample from station 20, 2550 m depth (GT8705st) was analyzed for chemical species mapping to calculate the average Mn oxidation state of the area. The result was compared to the Mn oxidation state of the same sample determined by bulk XANES at SSRL beamline 11-2, where the sample was cooled with liquid nitrogen, minimizing the beam damage. Although the areas of the filter that were irradiated by X-ray may not be the same between the two, the comparison is justifiable because a large enough area of the SSF filter was examined in both cases such that particle heterogeneity should be averaged out. The chemmap resulted in an average Mn oxidation state of 3.72, which is  $\sim 3\%$  higher than that determined from bulk XANES (3.61). The Mn(II) fractions were less than 9% in both analyses, while chemmap estimated less Mn(III) (10%) but more Mn(IV) (81%) than bulk XANES (28% and 66%, respectively). Since the offset between the oxidation states determined by chemmap and bulk XANES was smaller when the bulk XANES was collected in a cryostat, we suspect that the  $\sim 14\%$  offset between chemmap and  $\mu$ -XANES observed in Fig. 3b was largely caused by photoreduction of the samples during  $\mu$ -XANES analysis at SSRL beamline 2-3. We therefore conclude that the Mn oxidation state calculated by chemmap is relatively reliable, although it appears to overestimate Mn(IV) at the expense of Mn(III), leading to a slight ( $< 3\%$ ) overestimate of the average oxidation state. Therefore, for LSF samples, we focus on the discussion of Mn oxidation state rather than the relative fractions of Mn(II)/(III)/(IV). The standard

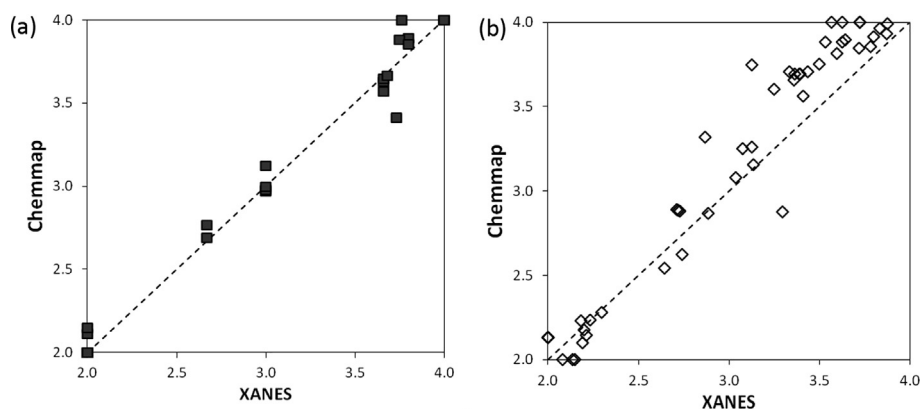


Fig. 3. Mn oxidation state of (a) Mn minerals and (b) hydrothermal plume particles determined by chemmap in comparison to those determined by XANES. The XANES-based Mn oxidation states in (a) are from Manceau et al. (2012, 2014). The dotted lines indicate the 1:1 line.

error of the regression slope ( $\pm 0.02$ ) in Fig. 3a was used as the uncertainty of chemmap-determined Mn oxidation states.

#### 2.4. Sorbed Mn standards

Several Mn(II)-sorbed particles were prepared to compare their EXAFS spectra to those from our Mn(II)-bearing samples from the hydrothermal plume. Mn(II)-sorbed POC was prepared using a method modified from Bargar et al. (2005a). A mixture of cultured phytoplankton (*Radiococcus planktonicus* and *Chlorella minutissima*) was filtered and washed with 0.2 mM ascorbate in 10 mM HEPES solution to remove any Mn oxides formed during culturing. After a short wash with Milli-Q water, the particles were resuspended and left in 1 mM Mn(II)Cl<sub>2</sub> added to 50 mM NaCl/10 mM HEPES solution overnight in darkness to allow Mn(II) adsorption onto the particles. Next day, the particles were filtered with 0.2  $\mu$ m polycarbonate filters and dried in a laminar flow bench.

For Mn-sorbed ferrihydrite, 2-line ferrihydrite was synthesized following the procedure from Schwertmann and Cornell (2000). For Mn(II)-sorbed PIC, we used foraminifera collected from sediment cores. In order to remove potential contamination of trace metal in natural foraminifera samples, they were first rinsed with Milli-Q water and methanol, cleaned with reductive and oxidative reagents, and finally leached in weak acid as in Martin and Lea (2002). The ferrihydrite and foraminifera were added to 0.2  $\mu$ m-filtered, surface seawater with low trace element concentrations amended with 1 mM Mn(II)Cl<sub>2</sub>, left suspended overnight in darkness, and then filtered the next day. The Mn-sorbed biogenic silica (bSi) was not examined because bSi concentrations were negligible in the studied hydrothermal plume (Lam et al., 2018). The XANES and EXAFS spectra of all absorption standards were obtained at SSRL beamline 11-2 in the liquid nitrogen cryostats. From the XANES analysis, the Mn sorbed onto ferrihydrite was found to have an oxidation state of 2.97. This is probably because sorbed Mn(II) was catalytically oxidized at the surface of ferrihydrite as previously reported (Davies and Morgan, 1989; Junta and Hochella, 1994).

### 3. RESULTS

#### 3.1. Spatial distribution and oxidation state of Mn in SSF particles

Distribution of Mn in SSF particles in the near-field plume agrees with the observation of Hoffman et al. (2018) where they found weak spatial correlations between Fe (as Fe oxyhydroxides), Mn, and Ca (as calcite) in the particles from stations 18 and 20. In these samples, Mn is sometimes co-located with Fe but also appears as Mn-only particles (Supp. Fig. 4a). Both Mn-only particles and Mn-Fe particles are also observed in the far-field plume, although they are rare and concentrations of Mn and Fe are lower compared to the near-field plume (Supp. Fig. 4b).

Overall, Mn in most SSF samples at all stations appears to be oxidized, with average oxidation states ranging between 3.2 and 3.7 (Fig. 4 and Supp. Table 1). One exception is the sample from 2500 m depth at station 18 that has an average oxidation state of 2.8 (GT8436st). The mineralogy of Mn in this sample could not be identified in this study (see Section 3.3), but since station 18 is located above the ridge axis, they may be materials near the venting site that have been entrained within the plume. A similar source has been proposed for the origin of organic matter in other hydrothermal plumes (Bennett et al., 2011; Breier et al., 2012; Bennett et al., 2015). At station 20, the Mn oxidation state increases from 3.4 at 2300 m depth to 3.7 at 2800 m depth (Fig. 4). However, below the plume, the Mn oxidation state of the particles decreases to 3.2 at 2900 m. Average Mn oxidation state within the plume (2200–2800 m, except the sample from 2500 m depth at station 18) is slightly higher at station 20 ( $3.6 \pm 0.1$ ) than at the other stations ( $3.5 \pm 0.1$ ,  $3.5 \pm 0.1$ ,  $3.3 \pm 0.1$  at stations 18, 21, and 25, respectively), but there is no clear difference between the near-field and far-field plume SSF particles (Fig. 4). Although the Mn oxidation state is similar, the fraction of Mn(III) in pMn is noticeably different between the near-field and far-field plumes (Fig. 5). Depth-averaged Mn(III) fractions in the plume particles are  $21 \pm 16\%$  and  $19 \pm 12\%$  at stations 18 and 20, respectively, but they

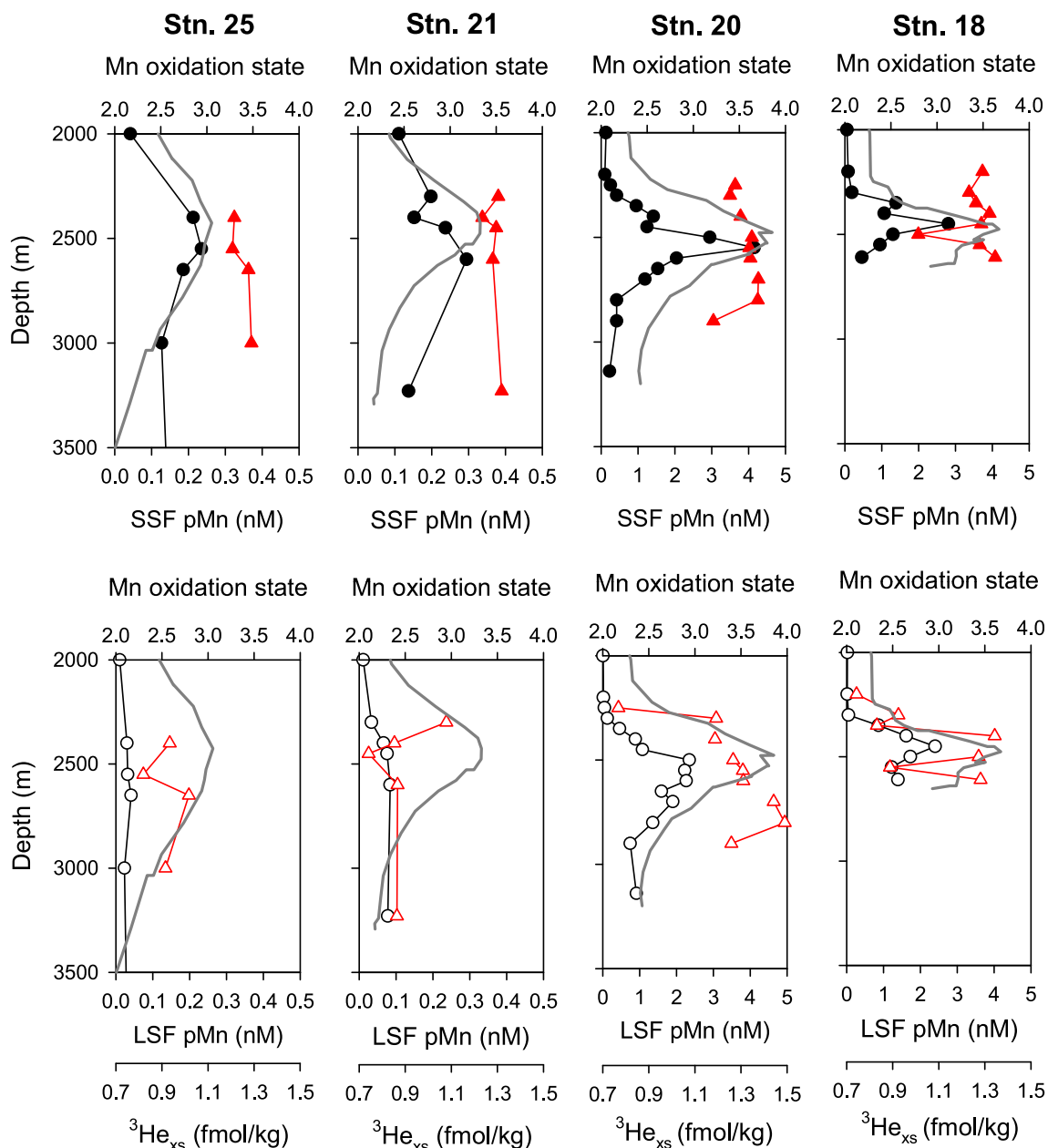


Fig. 4. Average Mn oxidation state (triangles) of SSF (top) and LSF (bottom) particles in the near-field (stations 18 and 20) and far-field (stations 21 and 25) plumes. The location of the hydrothermal plume is shown by increased excess  $^3\text{He}$  concentrations (fmol/kg) (grey lines) (Jenkins et al., 2018) and particulate Mn concentrations (nM) (circles). Note that pMn concentration scales are an order of magnitude higher at stations 18 and 20 than at stations 21 and 25. Panels are arranged so that distance from the ridge axis increases from right to left.

decrease to  $6 \pm 11\%$  and  $9 \pm 14\%$  at stations 21 and 25. The decrease in Mn(III) fractions in the far-field plume is compensated by an increase in Mn(II) and Mn(IV) fractions, mostly in Mn(II) (Fig. 5).

### 3.2. Spatial distribution and oxidation state of Mn in LSF particles

In the near-field plume, LSF pMn mostly occurs as hot-spots of small (tens of  $\mu\text{m}$ ) aggregates or large Fe- and Mn-rich aggregates that are hundreds of  $\mu\text{m}$  in size (Fig. 6a and

b). The large aggregates with Mn- and/or Fe-rich particles often appear with Cl (Figs. 6a, b, and 7a), indicating an association or aggregation of these particles with organic matter. The Cl is from salt in seawater that is retained within porous organic aggregates as samples dry. Since carbon fluorescent X-rays are too weak to be detected at the beamline we used, Cl was used as a tracer of organic matter aggregates. At stations 18 and 20, more large Fe- and Mn-rich aggregates are found at depths below the center of the plume, but they are not observed in the far-field plume (Fig. 6c and d).

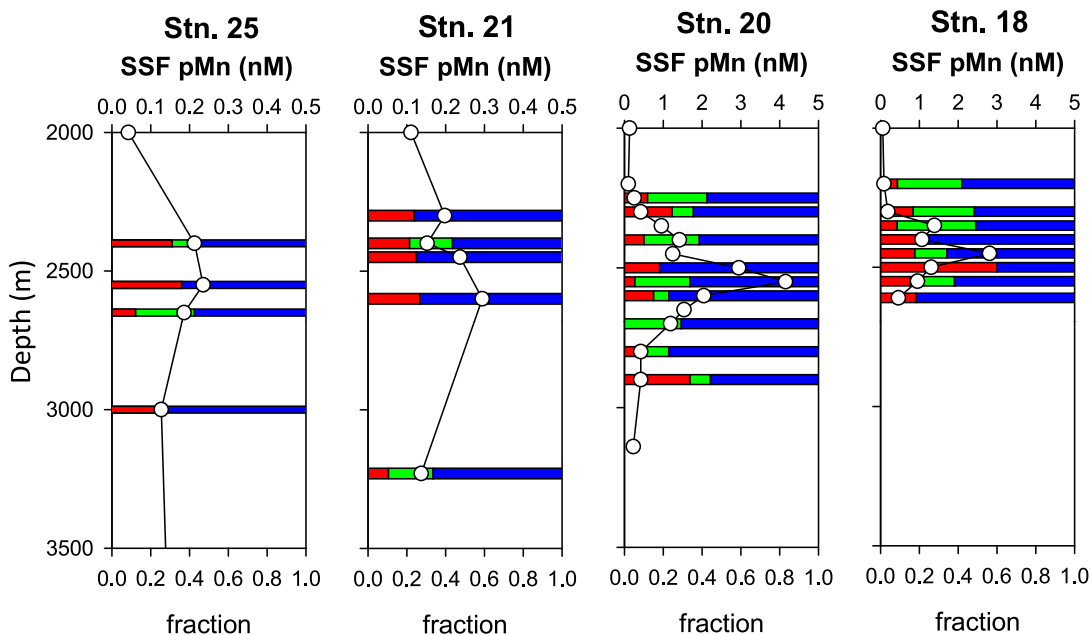


Fig. 5. Relative fractions of Mn(II), Mn(III), and Mn(IV) in SSF particles from the near-field (stations 18 and 20) and far-field (stations 21 and 25) plumes shown as bar graphs (red: Mn(II), green: Mn(III), blue: Mn(IV) on bottom x-axis). SSF pMn concentrations (nM) are shown as circles (top x-axis). Panels are arranged so that distance from the ridge axis increases from right to left. (For interpretation of the references to colour in this figure legend, the reader is referred to the web version of this article.)

At station 18, LSF pMn above the center of the plume is reduced (oxidation state  $<2.6$ ), but the LSF pMn around and below the center of the plume is oxidized (oxidation state  $\sim 3.5$ ) except at 2550 m depth (Fig. 4 and Supp. Table 2). All individual particles examined from the 2550 m depth sample (GT8435qp) were reduced (Supp. Table 2), and a unique particle type was also observed in this sample. These unique particles have moderate Mn but little Fe and Cl, and the Mn is dominated by Mn(II) and appears as a smooth and diffuse coating rather than as hotspots (Fig. 7b). At station 20, the Mn oxidation state of LSF particles increases with depth from 3.23 at 2300 m depth to 3.97 at 2800 m depth (Fig. 4). The increase in Mn oxidation state with depth was also observed in SSF particles at station 20 (Fig. 4 and Supp. Table 1), but it is more prominent in the LSF particles. Below the plume (2900 m), the Mn oxidation state of LSF particles decreases to 3.40 like it did in the SSF particles (Fig. 4), indicating that the oxidation process is slow outside of the plume.

The LSF pMn from the far-field plume mostly appears as small (tens of  $\mu\text{m}$ ) aggregates (Figs. 6c, d and 7c) and they appear infrequently. Unlike the small aggregates found in the near-field plume, Mn in these aggregates is reduced (Fig. 7c). Among 50 individual particles investigated at stations 21 and 25, 47 particles exhibit Mn oxidation state lower than 3 (Supp. Table 2). The average Mn oxidation state of LSF particles within the plume (2200–2800 m) at stations 21 ( $2.5 \pm 0.4$ ) and 25 ( $2.5 \pm 0.2$ ) is lower than those at stations 20 ( $3.4 \pm 0.6$ ) and 18 below 2400 m ( $3.2 \pm 0.5$ ) (Fig. 4). Even accounting for a potential slight ( $\sim 3\%$ ) overestimation of the oxidation state by chemmap (see Section 2.3.4), the difference is significant. The Mn in the

LSF particles at stations 21 and 25 is also considerably more reduced than those in the SSF particles at the same depths (Fig. 4), implying that the Mn in SSF and LSF particles are not exchanging rapidly in the far-field plume.

Very reduced Mn (oxidation state between 2.1 and 2.2) in the LSF particles is found at the upper boundary of the plume at stations 18 (2200 m) and 20 (2250 m) (Fig. 4). The Mn observed at these depths is often associated with organic aggregates or fecal pellets (discernible from their defined shapes) that contain relatively low concentrations of Fe and Mn (Fig. 7d). Given the depths at which they were found, these particles likely originated from the water column above. The C-rich, Fe-poor particles have been also found at the top of the plume (2350 m) at these stations (18 and 20) and were shown to be a mixture of plume materials and sinking POC from the overlying water column (Hoffman et al., 2018). Organic aggregates with low concentrations of Fe and Mn were also observed at other depths and stations (e.g., station 18, 2610 m and station 25, 2650 m) and were always associated with reduced Mn.

### 3.3. Mn mineralogy based on Mn EXAFS

Two SSF samples collected from the center of the near-field plume, GT8437st (station 18, 2450 m) and GT8705st (station 20, 2550 m), were analyzed for Mn by EXAFS in an attempt to identify Mn minerals appearing in the samples. The Mn in these samples is oxidized, with oxidation states of 3.48 and 3.61, respectively. The EXAFS spectra from these two samples were almost identical and show peaks at around  $k = 6.6$ ,  $k = 7.8\text{--}7.9$ , and  $k = 8.9 \text{ \AA}^{-1}$

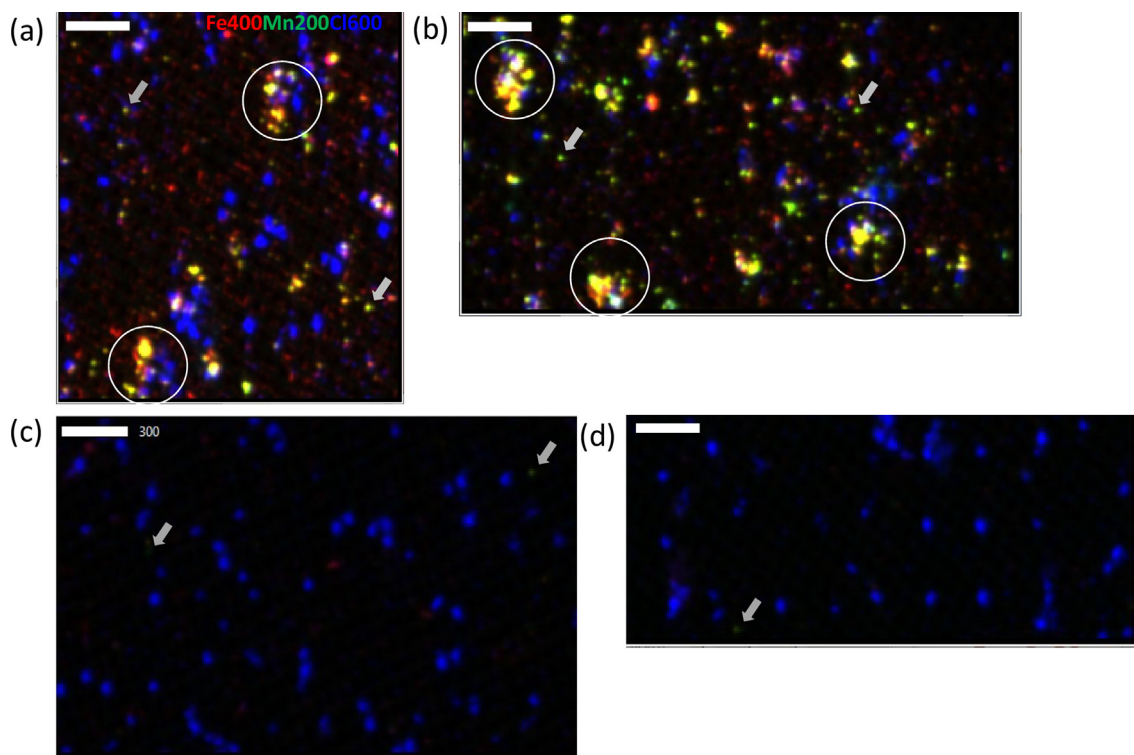


Fig. 6. “Coarse” X-ray fluorescence (XRF) tricolor maps of LSF particles from the near-field (a) station 18, 2500 m, (b) station 20, 2550 m, and far-field (c) station 21, 2600 m, (d) station 25, 2550 m plumes. Red, green, and blue represent Fe, Mn, and Cl, respectively. The color intensities scale with the element concentrations, with the white levels for each color set at 400 cps, 200 cps, and 600 cps for Fe (red), Mn (green), and Cl (blue), respectively, for all panels. Co-location of Fe and Mn appear yellow, Fe and Cl appear magenta, Mn and Cl appear cyan, and all three elements appear white. Examples of large ( $\sim 300 \mu\text{m}$ ) aggregates of Mn- and Fe-rich particles with organic matter (Cl) are shown in circles and small ( $\sim 50 \mu\text{m}$ ) Mn-containing aggregates by arrows. All scale bars are  $300 \mu\text{m}$ . (For interpretation of the references to colour in this figure legend, the reader is referred to the web version of this article.)

(Fig. 8). The peak at  $k = 7.8\text{--}7.9 \text{ \AA}^{-1}$  is broader and smaller than the peak of  $\delta\text{-MnO}_2$  appearing at  $k = \sim 8 \text{ \AA}^{-1}$ , and the  $k = \sim 8.9 \text{ \AA}^{-1}$  peak also appears at a lower  $k$  than that of  $\delta\text{-MnO}_2$  ( $k = \sim 9.1 \text{ \AA}^{-1}$ ) (Fig. 8). The location of these peaks suggests the presence of triclinic birnessites in the samples. Indeed, linear combination fitting of these EXAFS spectra shows that both samples have a significant amount of triclinic birnessite (Fig. 8). The spectra of GT8437st are best modeled with 16% pyroxmangite, 7% feitknechtite, 33% triclinic birnessite, and 44%  $\delta\text{-MnO}_2$  (R-factor = 0.115). Similarly, the spectra of GT8705st are best modeled with 9% hureaulite, 9% feitknechtite, 34% triclinic birnessite, and 48%  $\delta\text{-MnO}_2$  (R-factor = 0.139). Considering that triclinic birnessite contains 38 mol% of Mn(III) (Silvester et al., 1997), the Mn oxidation states of the samples are calculated to be 3.48 for GT8437st and 3.60 for GT8705st from the EXAFS spectra, which agrees with those calculated from the XANES spectra (3.48 and 3.61; Supp. Table 1).

In order to identify minerals with reduced Mn appearing in the samples, two samples were examined by EXAFS. One was an SSF sample from station 18, 2500 m depth (GT8436st), whose Mn oxidation state is 2.80 according to its determination by bulk XANES. The other sample was a single LSF particle found at 2550 m depth at station 18 (GT8435qp) with a smooth and diffuse coating of reduced Mn and little Fe and Cl (Fig. 7b). A  $10 \times 10 \mu\text{m}^2$

spot of this particle was analyzed for XANES and EXAFS, and the Mn oxidation state of the analyzed spot was 2.37. The EXAFS from the SSF and LSF samples show features at different  $k$  (Supp. Fig. 5), demonstrating that they contain different types of Mn minerals from each other. Removal of dissolved Mn(II) by adsorption onto other particles (Mandernack and Tebo, 1993) or sulfide formation (Breier et al., 2012) has been reported in some hydrothermal systems. However, neither of our sample spectra could be modeled with the sorption standards in our library, including Mn(II)-sorbed POC, Mn(II)-sorbed PIC, Mn-sorbed ferrihydrite, Mn sulfide, nor by other common Mn(II)-bearing minerals such as hureaulite, pyroxmangite, and rhodochrosite (Supp. Fig. 5). Therefore, at least two different Mn(II)-bearing minerals seem to exist in these hydrothermal plume particles, but they could not be identified in this study.

## 4. DISCUSSION

### 4.1. Mn cycling in the near-field plume

Within the hydrothermal plume at stations 18 and 20, Mn in SSF particles is dominated by oxidized Mn (Fig. 4). At station 18, the oxidized Mn in LSF particles appears only at depths below 2400 m (Fig. 4), but the

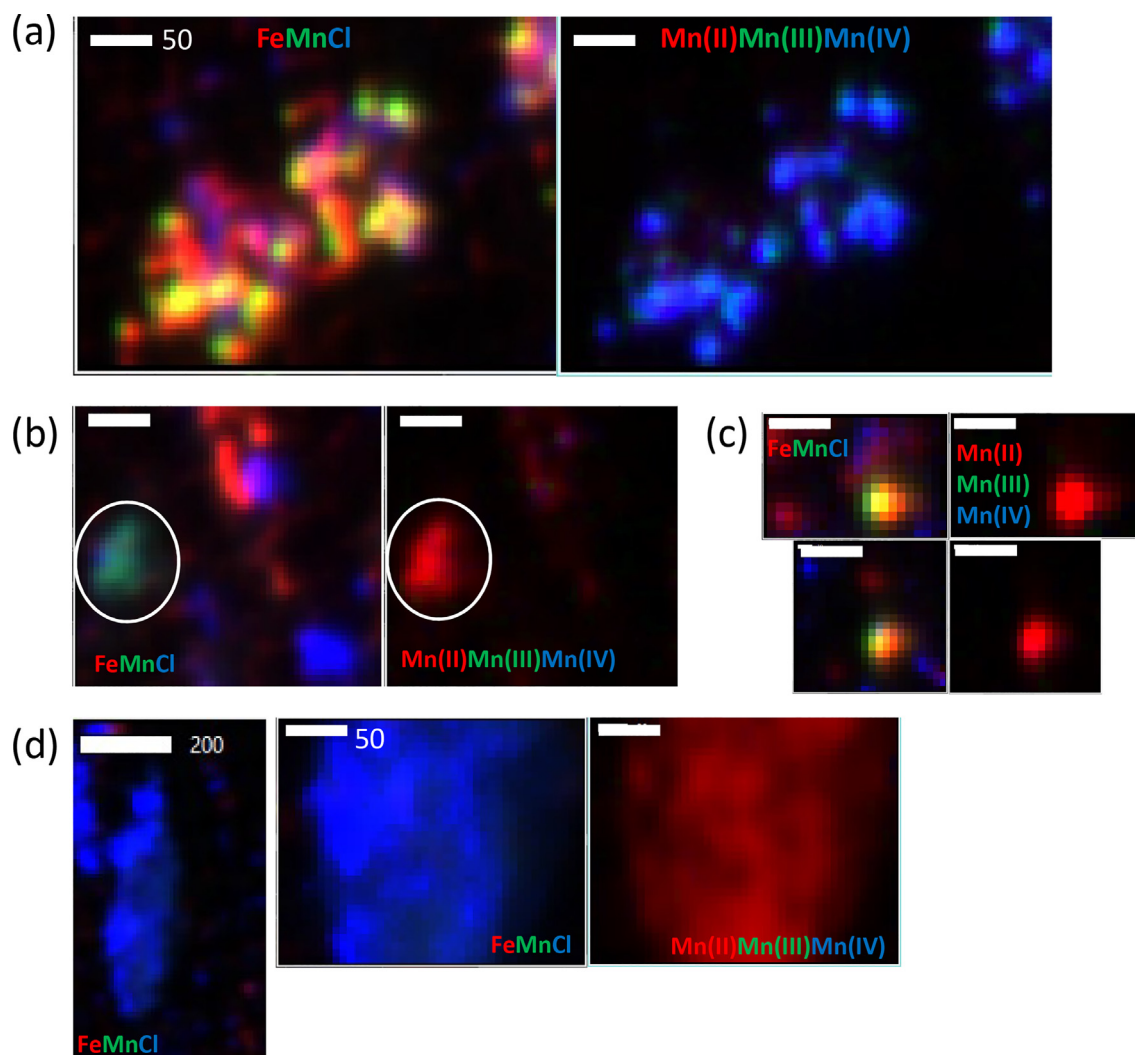


Fig. 7. Tricolor XRF maps (left) and chemmaps (right) of LSF particles from the hydrothermal plume: (a) large aggregates with oxidized Mn, Fe, and organic matter (Cl) from station 18, 2610 m, (b) a particle with smooth coating of reduced Mn from station 18, 2550 m, (c) small aggregates with reduced Mn from station 21, 2450 m, and (d) organic aggregates with low concentrations of reduced Mn from station 18, 2610 m. Colors in the XRF maps and chemmaps represent different elements (red = Fe, green = Mn, blue = Cl) and Mn speciation (red = Mn(II), green = Mn(III), blue = Mn(IV)), respectively. The maximum intensities of red, green, and blue are set to be equal within each image but vary between images to best represent how the relative contributions of each element and Mn species change between particle types. For example, in the XRF map in panel (d), the apparent absence of green for Mn simply indicates that Mn concentrations are much lower than Cl concentrations. The chemmap shows that there is Mn present, and it is all in the reduced form, Mn(II). Scale bars are 50  $\mu\text{m}$  unless otherwise indicated. (For interpretation of the references to colour in this figure legend, the reader is referred to the web version of this article.)

oxidized LSF pMn appears at a broader depth range at station 20. This result is consistent with the observation by Resing et al. (2015) that dMn is lost rapidly via oxidation to a particulate phase in the near-field plume.

At these stations, LSF particles make up  $\sim 25\%$  of the total suspended particulate matter in the plume (Lam et al., 2018), and this size partitioning extends to most elements, such that most trace elements are found mainly (70–80%) in SSF particles. However, Mn concentrations are similar between SSF and LSF particles, indicating that Mn contents in LSF particles are higher compared to the other elements (Lee et al., 2018; Supp. Fig. 6). Such an unusual size partitioning of pMn with a half in the LSF was only observed in the near-field hydrothermal plume. In

the near-field, vent fluids are diluted rapidly by deep-ocean seawater, and the turbulent mixing of the two accelerates aggregation of the particles that were entrained during the plume rise as well as those precipitating within the plume (Dymond and Roth, 1988; Adams et al., 2011; Bennett et al., 2011; Jiang and Breier, 2014). This results in aggregates of high Mn, Fe (Fe oxyhydroxides), and organic matter (traced by Cl) that are as big as several hundred  $\mu\text{m}$  in size (Figs. 6a, b and 7a). Cowen and colleagues showed that particulate Mn oxides in the Juan de Fuca Ridge hydrothermal plume often appear as metal-encrusted capsule bacteria (Cowen and Li, 1991), and suggested that the shape and sticky nature (polysaccharides) of the capsules may increase aggregation efficiency (Cowen,

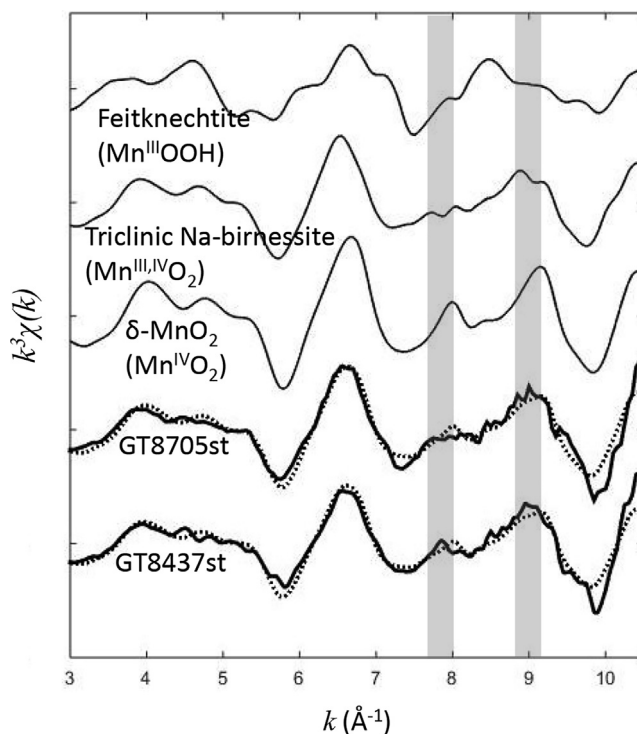


Fig. 8. Mn EXAFS spectra for three Mn oxide mineral standards (thin black lines) and two SSF particle samples from the near-field plume (thick black lines). The least squares combination fit to the samples are indicated in the dotted lines, and the fits include  $\sim 34\%$  triclinic birnessite and  $\sim 46\%$   $\delta$ - $\text{MnO}_2$  (see Section 3.3). The grey shaded areas highlight the regions of spectral difference between  $\delta$ - $\text{MnO}_2$  and triclinic birnessite.

1992). If Mn-oxidizing bacteria present in the 15°S EPR plume had similar properties, they would have also facilitated formation of large aggregates at stations 18 and 20. Even still, only Mn (and Co, see Section 4.3.1) is so highly partitioned to the LSF, so a mechanism is required that selectively enriches Mn (and Co) in the LSF particles and not other elements.

The precipitation of additional Mn in the LSF particles may be related to autocatalytic Mn oxide formation. Microbial Mn(II) oxidation primarily produces  $\delta$ - $\text{MnO}_2$ , a poorly crystalline phyllosilicate (a manganese oxide that consists of layers of edge-sharing  $\text{MnO}_6$  octahedra) in hexagonal symmetry (Bargar et al., 2000; Villalobos et al., 2003; Jurgensen et al., 2004; Bargar et al., 2005b; Webb et al., 2005b). This primary product is dominated by Mn(IV) oxides (Bargar et al., 2000). In the presence of dissolved Mn(II), the microbial oxidation reaction is followed by inorganic, autocatalytic oxidation in which dissolved Mn(II) adsorbed to the surface of the biogenic Mn oxide is oxidized while reducing Mn(IV) of the mineral to Mn(III) (Bargar et al., 2005a; Learman et al., 2011b). The increased Mn(III) in the octahedral sheet results in Jahn-Teller distortions, transforming (“ripening”) hexagonal birnessite into triclinic (or “pseudo-orthogonal”) birnessite (Lanson et al., 2002; Webb et al., 2005b; Learman et al., 2011b; Ling et al., 2018) when Mn(III) concentrations exceed  $\sim 25$  mol% (Ling et al., 2018). Learman et al. (2011b) further observed that the autocatalytic oxidation could not be sustained without continued formation of

fresh, biogenic Mn(IV) oxides because the reactivity of the Mn oxides decreases as Mn(III) increases in the mineral phase.

The EXAFS results of the two SSF samples from the near-field stations show that Mn in the samples are composed of  $\sim 34\%$  triclinic birnessite and  $\sim 46\%$   $\delta$ - $\text{MnO}_2$  (Fig. 8). This suggests that both biotic (microbial) and abiotic (autocatalytic) oxidation of Mn(II) occur actively in the near-field plume, and the autocatalytic reaction is as important as microbial oxidation in precipitating Mn oxides. The Mn(III) in the particles might also have resulted from reduction of Mn(IV) oxides by Fe(II) (Postma, 1985; Postma and Appelo, 2000), but the possibility is low due to rapid loss of vent-derived Fe(II) before the formation of Mn oxides. Measurable amounts of dFe(II) were only found at the bottom layers of station 18 (1.9 nM at 2550 m and 0.5 nM at 2625 m depth; Moffett et al., 2014), but even in these layers, dMn(II) concentrations are 7–24 times higher than dFe(II) (13.8 nM at 2550 m and 11.9 nM at 2625 m depth; Resing et al., 2015), suggesting that autocatalytic Mn(II) oxidation is more likely to occur than Fe(II) oxidation at the surface of Mn oxides. Manganese in the LSF particles is as oxidized as or even more oxidized than Mn in the SSF particles from corresponding depths and stations in the near-field plume (Fig. 4). Since autocatalytic Mn oxidation decreases Mn(IV) and increases Mn(III) contents in Mn oxides, highly oxidized Mn in the LSF particles implies that fresh microbial Mn oxidation also occurs within the LSF particles. Therefore, Mn in

the LSF particles is not just the result of aggregation of small pMn, but also of additional Mn oxide precipitation via microbial oxidation that is presumably followed by autocatalytic Mn oxidation.

Oxidation of soluble Fe(II) in the hydrothermal plume precipitates nanoparticulate Fe(III) oxyhydroxides in the colloidal (<0.2  $\mu\text{m}$ ) size fraction (Fitzsimmons et al., 2017), which then grow to a filterable particulate (>0.2  $\mu\text{m}$ ) size via adsorption to or aggregation with organic C, forming Fe(III) oxyhydroxide-C<sub>org</sub> composites (Fitzsimmons et al., 2017; Hoffman et al., 2018). The growth of these small Fe particles to the LSF particles (>51  $\mu\text{m}$ ) is thought to be controlled by general particle aggregation processes, i.e., collision with other particles. Since Fe oxyhydroxides scavenge many trace elements such as P and V, the distribution of these elements between SSF and LSF particles also follows that of pFe. For Mn, continuous microbial and autocatalytic Mn oxidation precipitates Mn oxides in both SSF and LSF particles. While small pMn also grows to large aggregates by general particle aggregation processes, additional Mn deposition onto LSF particles will cause Mn to be more concentrated in the LSF relative to Fe and other elements, resulting in the unusual size fractionation between the SSF and LSF particles that was previously reported.

#### 4.2. Mn cycling in the far-field plume

Resing et al. (2015) observed that dissolved Mn and excess  $^3\text{He}$  ( $^3\text{He}_{\text{xs}}$ ) concentrations are linearly correlated in the far-field hydrothermal plume from stations 21 to 36. As  $^3\text{He}_{\text{xs}}$  is conservative, i.e., only diluted by mixing without gain or loss, the correlation suggests that dissolved Mn(II) is almost conservative in the far-field plume, without being lost to a particulate phase via Mn oxide precipitation or adsorption. Thus, pMn found in the far-field plume likely originates from near-field materials. At far-field stations 21 and 25, average oxidation states of Mn in SSF particles are similar to or slightly lower than those in the near-field plume (Fig. 4), and their Mn(III) fractions are small (Fig. 5). Assuming that the Mn(III) fraction comes from triclinic birnessite, the results suggest that oxidized pMn in the SSF is transported to the far-field without further secondary (autocatalytic) Mn oxidation during transport. The Mn oxides with triclinic birnessite found at the near-field stations probably grew into fast-sinking large particles and were removed from the plume before reaching the far-field stations. The SSF pMn advected to the far-field plume may be a fraction of near-field SSF pMn that did not undergo autocatalytic oxidation, stayed small, and ripened to other Mn(IV) oxides that are less reactive (see Section 4.3).

The Mn in far-field LSF particles is significantly reduced compared to that of SSF particles from the same location (Fig. 4). The large difference in Mn oxidation states between these SSF and LSF particles implies that little or very slow aggregation occurs for pMn in the far-field plume. This agrees with the observation that the fraction of LSF pMn in total pMn decreases downstream of the plume (Supp. Fig. 6), which indicates that aggregation of

SSF to LSF pMn is slower than the removal of LSF pMn via sinking during plume dispersal (Supp. Fig. 6).

The Mn in LSF particles at the far-field stations is also far more reduced than at the near-field stations (Fig. 4), suggesting early and preferential loss of oxidized LSF pMn during westward advective transport. Several studies have suggested that concentrated microbial respiration can exhaust  $\text{O}_2$  inside organic aggregates, leading to the formation of anaerobic and even anoxic microenvironments in the particles (Allredge and Cohen, 1987; Ploug et al., 1997; Klawonn et al., 2015). In such environments, microbial dissimilatory Mn reduction may occur, and the reduced Mn (II) can be released as an aqueous phase (i.e., reductive dissolution), reoxidized, or reprecipitated as Mn(II)-bearing minerals (Thamdrup et al., 1994; Van Cappellen et al., 1998; Johnson et al., 2016). However, a recent modeling study showed that anaerobic microenvironments in aggregates are more likely to develop in regions where ambient  $\text{O}_2$  concentrations are low (e.g., oxygen minimum zones in the eastern tropical Pacific), but not in bathypelagic waters where  $\text{O}_2$  is sufficiently high (Bianchi et al., 2018). Moreover, labile particulate organic carbon concentrations at these depths are too low to exhaust  $\text{O}_2$  in the aggregates (Lam et al., 2018).

It is more likely that LSF Mn oxides in the hydrothermal plume were removed by gravitational sinking at the near-field stations and during transport to the far-field stations. Given that the large aggregates with oxidized Mn observed in the near-field plume were not found in the far-field plume (Figs. 6 and 7), we conclude that Mn oxides grow and aggregate quickly to large aggregates in the near-field and settle out of the plume before reaching station 21. The rapid removal of pMn in the near-field plume has been also suggested from a large decrease in pMn concentrations compared to  $^3\text{He}_{\text{xs}}$  (Fitzsimmons et al., 2017; Lee et al., 2018). Using a suite of synchrotron X-ray microscopy and spectroscopy techniques, Hoffman et al. (2018) showed that the materials in the fluffy layers (3178 m depth) at the bottom of station 20 are mostly from the upper water column and overlying hydrothermal plume. The pMn found in the fluffy layers was dominated by  $\delta\text{-MnO}_2$ , supporting the idea that Mn oxides settled out of the water column quickly before being transported to the far-field.

We suspect that the reduced Mn found in the far-field plume LSF particles is mostly associated with particles settled from the overlying water column, although its mineralogy could not be identified. The Mn associated with such particles seems to be mostly in a reduced form, either adsorbed or biologically bound to the particles, as observed in the LSF particles from the upper boundary of the plume (Mn oxidation state 2.1–2.2) (Fig. 4). This reduced pMn, settled from the overlying water column, is likely present both in the near-field and far-field plumes, but makes up a greater portion of the particles in the far-field due to a smaller contribution of the hydrothermal Mn oxides.

#### 4.3. Implication on the scavenging of trace elements

In the hydrothermal plume, Fe oxyhydroxides and Mn oxides scavenge trace elements (TE) and remove them from

the plume (German and Seyfried Jr., 2014 and references therein). The change in the pMn mineralogy and oxidation state between the near-field and far-field plumes may affect its adsorption capacity. In order to elucidate this, we used tracer-tracer plots which have been previously used to examine scavenging and removal occurring in hydrothermal plumes (German et al., 1990; German et al., 1991; Rudnicki and Elderfield, 1993). In these plots, if the concentrations of an element on the y-axis form a straight line with the concentrations of an element on the x-axis, both elements are mixed and diluted away from a hydrothermal source at the same rate. However, if the element concentrations on the y-axis are curved with respect to those on the x-axis, the y-axis element is scavenged onto the x-axis element (convex upward) or removed from the plume faster than the x-axis element (convex downward) during mixing. We plotted the particulate concentrations of elements that are known to be preferentially scavenged by Mn oxides: cobalt (Co), molybdenum (Mo), lead (Pb), and protactinium (Pa) (Mckenzie, 1980; Lee and Tebo, 1994; Moffett and Ho, 1996; Nelson et al., 1999a; Kashiwabara et al., 2011; Hayes et al., 2015), with respect to excess pMn and pFe concentrations in the near-field and far-field plumes (Figs. 9, 10, 12 and Supp. Fig. 7). Excess pMn ( $pMn_{xs}$ ) and pFe ( $pFe_{xs}$ ) are the pMn and pFe concentrations corrected for lithogenic fractions (see Lam et al., 2018), and are used interchangeably with Mn oxides and Fe oxyhydroxides.

#### 4.3.1. Scavenging of cobalt

In the studied southern EPR hydrothermal plume, particulate cobalt (pCo) behaves similarly to pMn in the near-field plume. Among the 15 elements analyzed, particulate Co and Mn are the only elements distributed almost evenly between SSF and LSF in the near-field plume (Lee et al., 2018). Particulate Co and excess pMn concentrations are also strongly correlated in both SSF and LSF particles in the near-field plume (Fig. 9a), suggesting that Co coexists with Mn oxides as a result of Co scavenging onto Mn oxides. In the far-field plume, however, the correlation between  $pMn_{xs}$  and pCo disappears as pCo concentrations fall to background levels while  $pMn_{xs}$  concentrations remain elevated in the plume (Fig. 9b).

The different Co-Mn correlations between near and far-field plumes result from the mechanism by which Co is oxidized. Cobalt was previously suggested to be directly co-oxidized by Mn-oxidizing bacteria (Lee and Tebo, 1994; Moffett and Ho, 1996). However, later it was found that soluble Co(II) is sorbed onto the surface of Mn oxides, and then indirectly oxidized to insoluble Co(III) oxides (Murray et al., 2007; Tanaka et al., 2013) using Mn in the mineral as an oxidant, i.e., reducing Mn(IV) in the mineral to Mn(III) (Crowther et al., 1983). This process is similar to the autocatalytic oxidation of Mn(II) by freshly-formed Mn(IV) oxides discussed in Section 4.1, and soluble Mn(II) and Co(II) may even compete for the fresh Mn(IV) oxides to be oxidized (Murray et al., 2007). Thus, freshly-formed Mn oxides in the near-field plume were used to oxidize soluble Co (as well as autocatalyze further oxidation of Mn(II)), leaving pMn with a higher proportion of Mn(III) (with pCo(III)) in the near-field plume. The absence of any Mn-

Co correlation in the far-field plume suggests that: (1) Mn oxides with higher Co contents that were present in the near-field plume were mostly removed during transport and (2) further scavenging of Co did not occur, at least not at a noticeable rate, in the far-field plume. The little Co scavenging in the far-field plume could be partly due to low labile Co (LCo, unbound and weakly bound to organic ligands) concentrations in the ambient seawater. Dissolved Co concentrations in the deep South Pacific were between 20–40 pM, but most of it was strongly bound to organic ligands (Hawco et al., 2016). The LCo in deep waters was almost undetectable (detection limit: 3.6 pM), except at station 18 where the LCo concentration was elevated up to 14 pM at depths between 2350 m and 2500 m, indicating hydrothermal inputs (Hawco et al., 2016). Such LCo seemed to be quickly scavenged near the ridge, however, and the LCo concentration dropped to background levels at station 20 and remained low in the far-field plume. Another reason for little Co scavenging in the far-field plume is the lack of or extremely slow biogenic Mn oxide formation. Since Co oxidation occurs via Mn(IV) oxides, similar to autocatalytic Mn(II) oxidation, the absence of fresh Mn(IV) oxide formation in the far-field plume also hinders scavenging of Co via oxidative precipitation.

#### 4.3.2. Scavenging of molybdenum

In a previous study, Ho et al. (2018) suggested that Mo is scavenged to both  $pFe_{xs}$  and  $pMn_{xs}$  in the near-field plume based on pMo-p $Fe_{xs}$  and pMo-p $Mn_{xs}$  plots of the SSF particles. However, close inspection of these plots reveals that SSF pMo-p $Fe_{xs}$  is in fact slightly convex downward (Supp. Fig. 7a), while SSF pMo-p $Mn_{xs}$  is linear (Fig. 9c and Supp. Fig. 7c). In the LSF particles, it is more obvious that pMo forms a straight line with respect to  $pMn_{xs}$  (Fig. 9c) but not with respect to  $pFe_{xs}$  (Supp. Fig. 7b, d), indicating that Mo is adsorbed onto pMn rather than pFe. The observed correlations in the pMo-p $Fe_{xs}$  plots are merely a reflection of the  $pMn_{xs}$ - $pFe_{xs}$  relationship (Supp. Fig. 7e, f) because Mo is associated with pMn. The Mo is adsorbed onto pMn with the same pMo:p $Mn_{xs}$  slope for the SSF and LSF, although there appears to be a pool of pMo in the SSF (a positive y-intercept) that is not in the LSF (Fig. 9c and Supp. Fig. 7c, d).

The dominant host phase of Mo in natural ferromanganese oxides has been under debate, but in recent years it is commonly thought to be Mn oxides (Barling and Anbar, 2004; Wasylenki et al., 2008). The preferential scavenging of Mo onto Mn oxides over Fe oxyhydroxides is attributed to different adsorption mechanisms for Mo onto the Mn and Fe minerals (Kashiwabara et al., 2011; Tanaka et al., 2018). In the oxic ocean, dissolved Mo (dMo) exists dominantly as molybdate ( $MoO_4^{2-}$ ), which is an oxyanion. Oxyanions (e.g.,  $PO_4^{3-}$ ) are often attracted electrostatically to Fe oxyhydroxides and form outer-sphere complexes because the surface charge of  $Fe(OH)_3$  is slightly net positive, whereas that of  $\delta$ - $MnO_2$  is net negative at seawater pH (Kashiwabara et al., 2011). While molybdate can be attracted to Fe oxyhydroxides like other oxyanions under certain conditions, Mo is dominantly adsorbed to Mn oxides at modern seawater pH and dMo concentrations

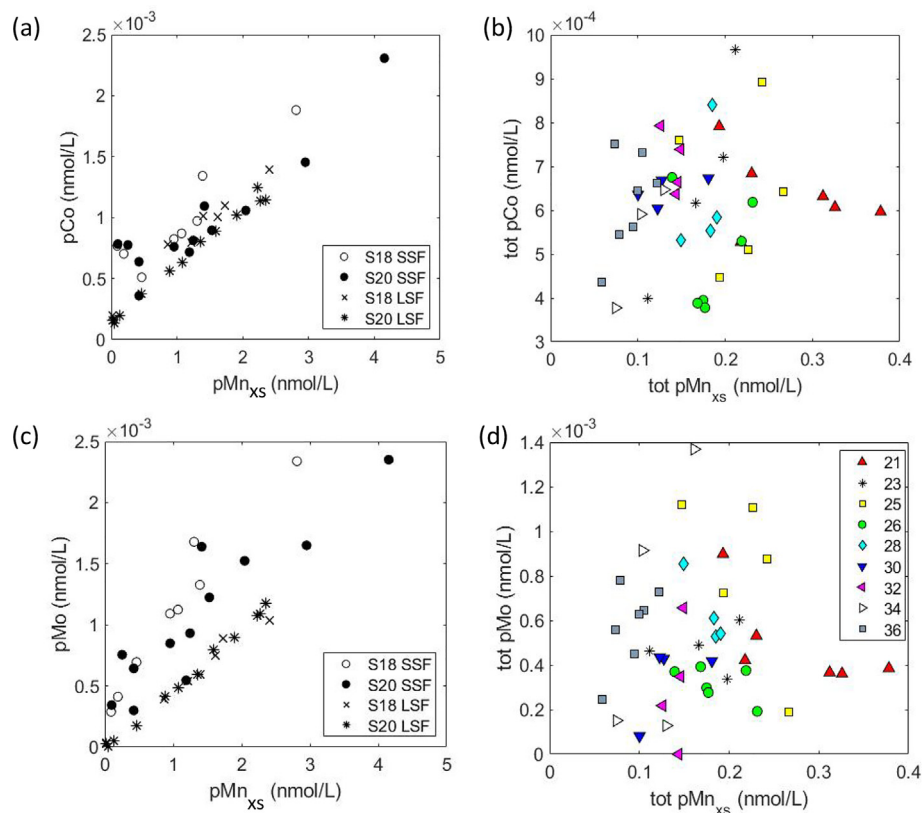


Fig. 9. Correlation between pCo, pMo and excess pMn at stations in the near-field (a and c) and far-field (b and d) plumes. Total (SSF + LSF) particle data are shown for the far-field plume. Station numbers for the data are shown in the figure legend.

( $\sim 0.11 \mu\text{mol/L}$ ) (Kashiwabara et al., 2011). Under such conditions, the empty  $d^0$  electron configuration and appropriate ionic radius of  $\text{Mo}^{6+}$  leads to its adsorption in a distorted octahedral coordination, with inner-sphere complexes between  $\text{Mo}^{6+}$  and the  $-\text{O}^-/-\text{OH}$  groups on the Mn oxide surface (Tanaka et al., 2018). This complex is more stable and therefore preferred than the outer-sphere complex that a molybdate anion forms to an Fe oxyhydroxide surface (Kashiwabara et al., 2011).

As observed with Co, the correlation between pMo and pMn<sub>xs</sub> in both size fractions disappears in the far-field plume (Fig. 9d), implying that Mn oxides with high Mo contents rapidly settled out near the ridge and further Mo scavenging did not occur in the far-field plume. The lack of Co scavenging in the far-field plume was ascribed in Section 4.3.1 to the lack of or reduced in-situ biogenic Mn oxidation and low LCo levels in the far-field. However, this is not the case for Mo because Mo scavenging does not necessarily need freshly-formed Mn oxides as the scavenging occurs via adsorption, not oxidative precipitation, and dMo is also not depleted in the far-field plume (Ho et al., 2018). As the LSF pMn in the far-field plume is mostly in the Mn(II) form rather than as Mn oxides (Fig. 4), these particles would not be expected to scavenge Mo. The SSF particles in the far-field appear to have oxidized Mn (Fig. 4), but their Mn(III) fractions are lower than for those in the near-field (Fig. 5 and Supp. Table 1). We suspect that far-field SSF pMn is composed of Mn minerals of lower

reactivity that cannot adsorb Mo as effectively as the Mn oxides in the near-field plume. Metal sorption properties of Mn oxides are known to be largely affected by their structure, Mn(III) contents, and vacancies (Nico and Zasoski, 2000; Zhao et al., 2009; Landrot et al., 2012), and a change in such properties may have reduced the reactivity of Mn oxides in the far-field plume. Unfortunately, this question remains unresolved because we were unable to obtain EXAFS data of adequate quality from the dilute far-field plume particles.

#### 4.3.3. Scavenging of lead

Unlike Co and Mo, which have adsorption mechanisms specific to Mn oxides, Pb can be adsorbed to both Fe oxyhydroxides and Mn oxides by forming inner-sphere complexes between the hydroxyl ions on the mineral surface and the Pb ions (Bargar et al., 1997; Villalobos et al., 2005). Preferential adsorption of Pb onto Mn oxides rather than Fe oxyhydroxides has been observed in many natural environments (Mckenzie, 1980; Nelson et al., 1999b; Wilson et al., 2001). However, in the hydrothermal plume from the southern EPR, Pb appears to be associated with pFe<sub>xs</sub> rather than pMn<sub>xs</sub> (Fig. 10). In the near-field plume, pPb is linearly correlated with pFe in both the SSF and LSF, indicating that Pb is associated with pFe<sub>xs</sub> and mixed away from the source at the same rate (Fig. 10d). In the far-field plume, the correlations between pPb and pMn<sub>xs</sub> or pFe<sub>xs</sub> are less clear in the tracer-tracer plot because of the

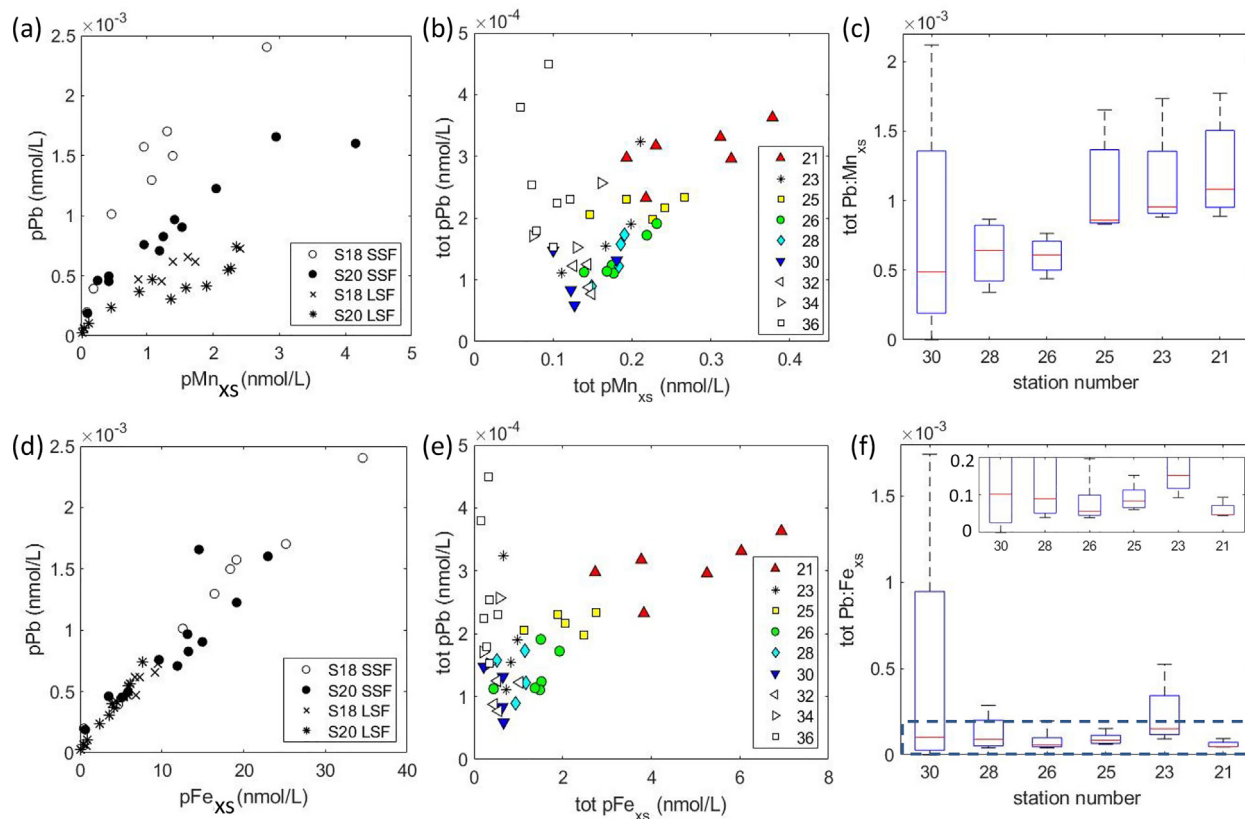


Fig. 10. Correlations between pPb and excess pMn (or pFe) concentrations at stations in the near-field (a and d) and far-field (b and e) plumes. Changes in the background-removed, total particulate Pb:Mn<sub>XS</sub> (c) and Pb:Fe<sub>XS</sub> (f) ratios (nmol:nmol) in the far-field plume are shown with box plots. The inset in panel (f) shows magnification of the dashed area. On each box, the central mark indicates the median, and the bottom and top edges of the box indicate the 25th and 75th percentiles, respectively. The whiskers extend to the maximum and minimum data points. Far-field particle data are shown as total (SSF + LSF). As shown in (b) and (e), particulate Pb concentrations beyond station 30 are elevated because of potential anthropogenic Pb contamination and thus were not included in (c) and (f).

scatter in the data (Fig. 10b, e). Thus, we also plotted particulate Pb:Fe<sub>XS</sub> and Pb:Mn<sub>XS</sub> ratios in the plume (Fig. 10c, f), which were calculated after subtracting background values (assumed to be the minimum values of the pPb, pFe<sub>XS</sub>, and pMn<sub>XS</sub> in the entire plume) from each datapoint. The slight upward curvature in the pPb vs pFe<sub>XS</sub> tracer plots (Fig. 10e), and slight increase in particulate Pb:Fe<sub>XS</sub> ratios between stations 21 and 30 (Fig. 10f) suggest that Pb is slowly, yet continuously scavenged onto pFe<sub>XS</sub> within the westward-flowing plume. The pPb concentrations at the westernmost stations (stations 34 and 36) are higher than those expected from the trend (Fig. 10b, e). Similarly, increasing dissolved Pb (dPb) concentrations have been found within the plume west of station 30, and this was attributed to the mixing of diluted plume water with deep mid-Pacific waters containing higher dPb due to anthropogenic Pb inputs (Boyle et al., 2020). In contrast, between stations 21 and 30, particulate Pb:Mn<sub>XS</sub> ratios decrease with increasing station number (Fig. 10c), suggesting that pPb is lost faster than pMn during plume transport. Since pFe is lost faster than pMn in the far-field plume (Supp. Fig. 8), the faster removal of pPb relative to pMn is predictable given that Pb is associated with pFe. The scavenging of dPb by pFe<sub>XS</sub> is also supported by the data collected from

GEOTRACES GO-Flo sampling bottles (Cutter and Bruland, 2012). The GO-Flo bottle dPb concentrations often show minima at depths ~500 m below the <sup>3</sup>He<sub>XS</sub> maximum (Boyle et al., 2020). In the particle (>0.45 μm) data collected from the same GO-Flo bottles, the pFe maximum was also found 100–350 m deeper than the <sup>3</sup>He<sub>XS</sub> maximum, whereas the pMn maximum remained close in depth to the <sup>3</sup>He<sub>XS</sub> maximum over the plume length (Fitzsimmons et al., 2017). Such depth difference was only observed in the GO-Flo data where samples were collected at high depth resolution and was not found in our pump particle data or dissolved <sup>210</sup>Pb concentration data (Niedermiller and Baskaran, 2019).

The affinity of particles to scavenge an element, X, is described by its bulk partition coefficient,  $K_d(X)$ , in units  $\frac{X \text{ per g particles}}{X \text{ per g seawater}}$ . It is defined as  $K_d(X) = \frac{X_{\text{ads}}^p}{X^d} \times \frac{1}{\text{SPM}} = K(X) \times \frac{1}{\text{SPM}}$ , where  $X_{\text{ads}}^p$  and  $X^d$  represent the concentrations (or activities) of an element, X, in the particulate (adsorbed) and dissolved phases (g particulate (adsorbed) × per g seawater and g dissolved × per g seawater), respectively, and SPM is the suspended particulate matter concentration (g SPM per g seawater). End-member  $K_d$  values have been calculated for a variety of trace elements and

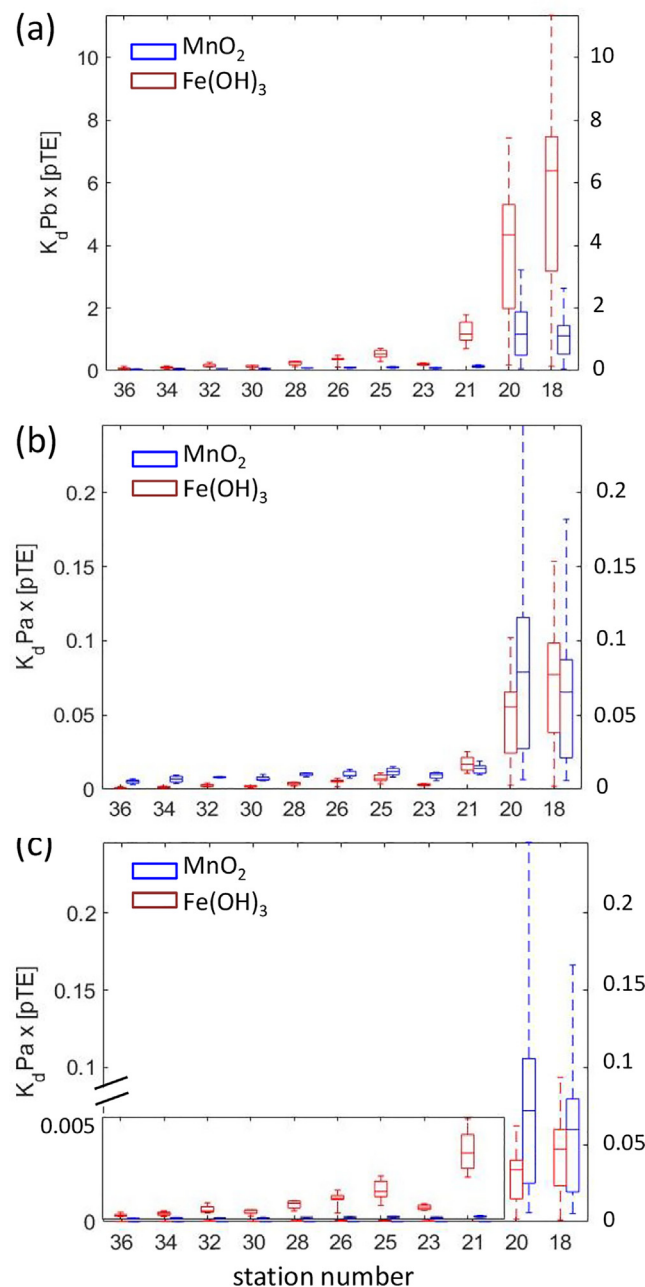


Fig. 11. Box plot of  $K_d^{\text{MnO}_2}$  (blue) and  $K_d^{\text{Fe(OH)}_3}$  (red) calculated for (a) Pb using end-member  $K_d$  values from Bam et al. (2020) (derived from the entire Arctic section) and for  $^{231}\text{Pa}$  using the end-member  $K_d$  values derived from (b) the entire EPZT section and (c) the near-field and far-field plume data exclusively. Total (SSF + LSF)  $\text{MnO}_2$  and  $\text{Fe(OH)}_3$  concentrations were used to calculate  $K_d^{\text{MnO}_2}$  and  $K_d^{\text{Fe(OH)}_3}$  for Pb. For  $^{231}\text{Pa}$ , only SSF data were used for calculation because LSF  $^{231}\text{Pa}$  data are unavailable at most far-field stations. On each box, the central mark indicates the median, and the bottom and top edges of the box indicate the 25th and 75th percentiles, respectively. The whiskers extend to the maximum and minimum data points. (For interpretation of the references to colour in this figure legend, the reader is referred to the web version of this article.)

isotopes (TEIs) using a linear regression technique (Hayes et al., 2015; Lamborg et al., 2016; Tang et al., 2017; Bam et al., 2020). End-member  $K_d$  values of Pb for six major particle phases (calcium carbonate, particulate organic matter, biogenic opal, lithogenic material, authigenic Fe oxyhydroxides and Mn oxides) that make up the SPM were calculated using dissolved and particulate  $^{210}\text{Pb}$  concentra-

tions and particle composition data from the U.S. GEOTRACES Arctic cruise (GN01 section) (Bam et al., 2020). A significant end-member  $K_d(\text{Pb})$  for  $\text{Fe(OH)}_3$ ,  $K_d^{\text{Fe(OH)}_3}(\text{Pb})$ , could be calculated for LSF particles only, whereas  $K_d(\text{Pb})$  for  $\text{MnO}_2$ ,  $K_d^{\text{MnO}_2}(\text{Pb})$ , could be calculated for SSF, LSF, and total (SSF + LSF) particles. This may

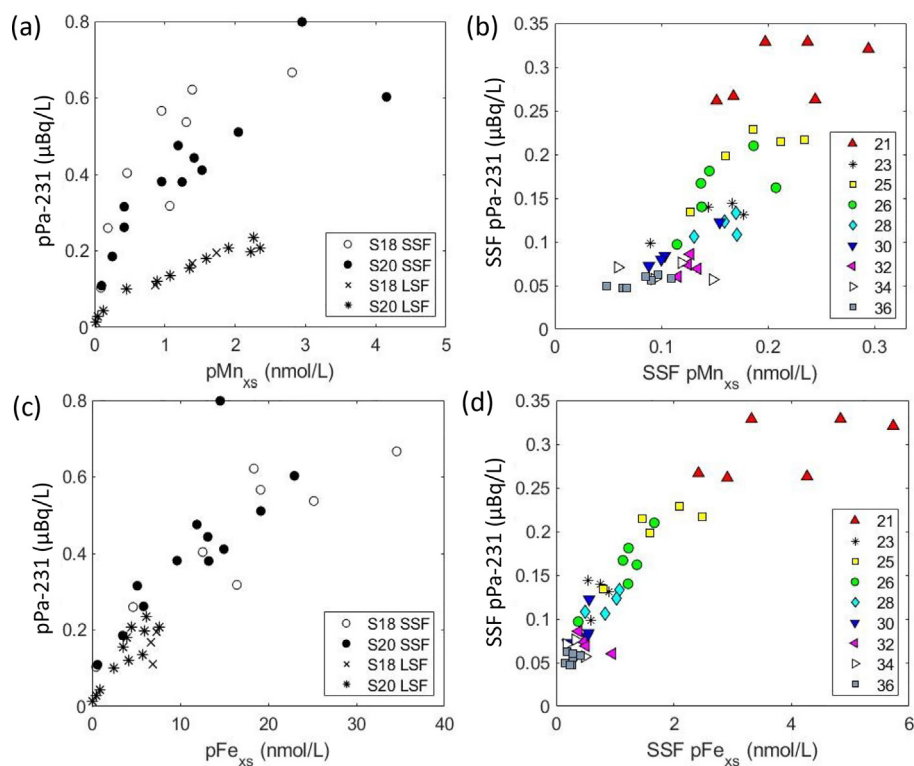


Fig. 12. Correlations between SSF and LSF  $p^{231}\text{Pa}$  and  $p\text{Mn}_{\text{xs}}$  (or  $p\text{Fe}_{\text{xs}}$ ) at stations in the near-field (a and c) and far-field (b and d) plumes. Far-field plume data are shown for SSF particles only because the LSF  $p^{231}\text{Pa}$  data are unavailable due to low concentrations.

simply reflect the higher abundance of  $\text{MnO}_2$  than  $\text{Fe}(\text{OH})_3$  particles in the Arctic basin (Xiang and Lam, 2020). Since no significant difference was found between the  $K_d^{\text{MnO}_2}(\text{Pb})$  for SSF, LSF, and total particles (Bam et al., 2020), we compare  $K_d^{\text{MnO}_2}(\text{Pb})$  for total particles to the  $K_d^{\text{Fe}(\text{OH})_3}(\text{Pb})$  calculated from the LSF particles. The calculated  $K_d(\text{Pb})$  is about two times higher for  $\text{MnO}_2$  ( $581.1 \times 10^7 \text{ L/kg}$  or  $595.6 \times 10^7 \text{ g/g}$ ; calculated from total particles) than for  $\text{Fe}(\text{OH})_3$  ( $240.9 \times 10^7 \text{ L/kg}$  or  $246.9 \times 10^7 \text{ g/g}$ ; calculated from LSF particles) (Bam et al., 2020), indicating that Mn oxides ( $\text{MnO}_2$ ) have a greater affinity than Fe oxyhydroxides ( $\text{Fe}(\text{OH})_3$ ) to scavenge Pb. However, in the studied hydrothermal plume,  $p\text{Fe}$  concentrations are an order of magnitude higher than  $p\text{Mn}$ . Thus,  $p\text{Fe}$  provides more reaction sites that Pb can adsorb to, which may offset  $\text{Fe}(\text{OH})_3$  having a smaller affinity than  $\text{MnO}_2$  to scavenge Pb. We calculated the product of the end-member  $K_d(\text{Pb})$  and the particle concentration for  $\text{Fe}(\text{OH})_3$  and  $\text{MnO}_2$ , or  $K_d^{\text{Fe}(\text{OH})_3}(\text{Pb})$  and  $K_d^{\text{MnO}_2}(\text{Pb})$ , to show how much Pb is partitioned to each of these particle phases for the same dissolved Pb ( $\text{Pb}^{\text{d}}$ ) concentration. Indeed, the result shows  $K_d^{\text{Fe}(\text{OH})_3}(\text{Pb}) = K_d^{\text{Fe}(\text{OH})_3}(\text{Pb}) \times [\text{pFe}(\text{OH})_3]$  is up to an order of magnitude higher than  $K_d^{\text{MnO}_2}(\text{Pb}) = K_d^{\text{MnO}_2}(\text{Pb}) \times [\text{pMnO}_2]$  over the entire plume length (Fig. 11a), supporting the idea that Pb has a higher chance of being scavenged by  $\text{Fe}(\text{OH})_3$  rather than by  $\text{MnO}_2$  in this hydrothermal plume.

#### 4.3.4. Scavenging of protactinium-231 ( $^{231}\text{Pa}$ )

The scavenging mechanism of  $^{231}\text{Pa}$  onto the mineral phases has not been clearly documented, but similar to Pb,  $^{231}\text{Pa}$  is known to be scavenged by both Mn oxides and Fe oxyhydroxides with a higher affinity for  $\text{MnO}_2$  (Hayes et al., 2015). In the near-field of the studied hydrothermal plume, SSF  $p^{231}\text{Pa}$  appears to be positively correlated to both  $p\text{Fe}_{\text{xs}}$  and  $p\text{Mn}_{\text{xs}}$  at first glance (Fig. 12a, c), with an almost straight line ( $p\text{Fe}_{\text{xs}}$ ) or a convex upward shape ( $p\text{Mn}_{\text{xs}}$ ). However, in the LSF,  $p^{231}\text{Pa}$  is almost linearly correlated with  $p\text{Mn}_{\text{xs}}$  but not with  $p\text{Fe}_{\text{xs}}$  (Fig. 12a, c). Why might there be a relationship between  $p^{231}\text{Pa}$  and  $p\text{Fe}_{\text{xs}}$  in the SSF but not the LSF? If we assume that  $^{231}\text{Pa}$  is associated primarily with pMn, the almost linear  $p^{231}\text{Pa}$ - $p\text{Fe}_{\text{xs}}$  correlation in the SSF (Fig. 12c) can be explained by a combination of the convex downward shape of  $p\text{Mn}_{\text{xs}}$ - $p\text{Fe}_{\text{xs}}$  (Supp. Fig. 7e) and the convex upward shape of  $p^{231}\text{Pa}$ - $p\text{Mn}_{\text{xs}}$  in the SSF (Fig. 12a). In other words, the apparent relationship between  $p^{231}\text{Pa}$  and  $p\text{Fe}_{\text{xs}}$  in the SSF may actually be a reflection of the underlying relationship between  $p^{231}\text{Pa}$  and  $p\text{Mn}_{\text{xs}}$ , and the relationship between  $p\text{Mn}_{\text{xs}}$  and  $p\text{Fe}_{\text{xs}}$ . Similarly, the poor relationship between  $p\text{Mn}_{\text{xs}}$ - $p\text{Fe}_{\text{xs}}$  in the LSF (Supp. Fig. 7f) would result in the weak relationship between  $p^{231}\text{Pa}$  and  $p\text{Fe}_{\text{xs}}$  in the LSF if  $^{231}\text{Pa}$  is bound to pMn. Thus, we suggest that  $^{231}\text{Pa}$  is mainly scavenged by pMn in the near-field plume, which is supported by Pavia et al. (2018) where they found the bulk partition coefficient of  $^{231}\text{Pa}$  ( $K_d(\text{Pa})$ ) at the

near-field stations to be similar to the end-member  $K_d(\text{Pa})$  for  $\text{MnO}_2$  ( $K_d^{\text{MnO}_2}(\text{Pa})$ ) derived from the U.S. GEOTRACES North Atlantic Zonal Transect (NAZT) cruise (GA03 section) data (Hayes et al., 2015).

In Fig. 12a, it is interesting that the near-field  $p^{231}\text{Pa}$ - $p\text{Mn}_{\text{xs}}$  plots have different shapes and slopes in the two particle size fractions: convex upward in the SSF and almost linear in the LSF, and the slopes are lower in the LSF. For both  $p^{231}\text{Pa}$  and  $p\text{Mn}_{\text{xs}}$ , the highest and lowest concentrations occur at the center and the upper boundary of the plume at each station, respectively. Since non-plume seawater has higher dissolved  $^{231}\text{Pa}$  ( $d^{231}\text{Pa}$ ) and lower  $p\text{Mn}$  than plume water, the curvature in the SSF particles implies that  $d^{231}\text{Pa}$  is continuously (and rapidly) scavenged onto hydrothermal-derived  $p\text{Mn}$  during the mixing of the two waters within the plume depth range. The scavenging of  $d^{231}\text{Pa}$  onto the LSF  $p\text{Mn}$  may be slower and thus have less curvature because the surface area to volume ratio is smaller in the LSF than the SSF particles. The different SSF and LSF slopes may be related to their residence times. Because small particles sink more slowly than large particles, the SSF particles are likely a mixture of what is precipitated in situ (formed at each station) and what was transported from upstream, whereas LSF particles are more likely to be formed in situ. As the SSF particles from upstream are already enriched in  $^{231}\text{Pa}$  due to continuous scavenging during transport, addition of these SSF particles would elevate the  $^{231}\text{Pa}:\text{Mn}_{\text{xs}}$  ratios in the SSF particles (higher slope) compared to the LSF particles.

In the far-field plume SSF particles, the  $p^{231}\text{Pa}$ - $p\text{Mn}_{\text{xs}}$  correlation is convex downward (Fig. 12b), whereas the SSF  $p^{231}\text{Pa}$ - $p\text{Fe}_{\text{xs}}$  correlation is convex upward (Fig. 12d). Therefore, in the far-field plume,  $^{231}\text{Pa}$  seems to be continuously scavenged by  $\text{Fe}(\text{OH})_3$ , while  $\text{Fe}(\text{OH})_3$  loaded with  $^{231}\text{Pa}$  is lost faster than  $p\text{Mn}$  during transport (Supp. Fig. 8). Dissolved  $^{231}\text{Pa}$  in the plume continuously grows in from the radioactive decay of  $^{235}\text{U}$  in seawater, causing the supply of  $d^{231}\text{Pa}$  to be uniform along the plume. The observed  $d^{231}\text{Pa}$  activities increase from stations 20 to 36 because scavenging intensity decreases westward as hydrothermal particles are diluted (Pavia et al., 2018). Pavia et al. (2018) suggested continuous scavenging of  $d^{231}\text{Pa}$  in the far-field plume based on a mass balance model, which is consistent with our observation in Fig. 12d. They further showed that bulk  $\log(K_d)$  (g/g) of  $^{231}\text{Pa}$  calculated for the SSF decreases from  $\sim 8.0$  in the near-field plume, which is similar to the end-member  $K_d^{\text{MnO}_2}(\text{Pa})$  derived by Hayes et al. (2015) ( $\sim 8.3$ ; Table 1), to  $\sim 7.1$  in the far-field at station 30, which is similar to the end-member  $K_d^{\text{Fe}(\text{OH})_3}(\text{Pa})$  ( $\sim 7.5$ ), although the fractionation factor of

$^{230}\text{Th}$  to  $^{231}\text{Pa}$ ,  $\left(F\left(\frac{\text{Th}}{\text{Pa}}\right) = \frac{K_d(\text{Th})}{K_d(\text{Pa})}\right)$ , was closer to that of  $\text{MnO}_2$  (5.5) than of  $\text{Fe}(\text{OH})_3$  (11.2) at most depths within the hydrothermal plume (ranging from  $\sim 4$  to 13).

In order to explain the preferential scavenging of  $^{231}\text{Pa}$  by  $p\text{Mn}$  in the near-field plume and by  $p\text{Fe}$  in the far-field plume,  $K^{\text{MnO}_2}(\text{Pa})$  and  $K^{\text{Fe}(\text{OH})_3}(\text{Pa})$  were calculated, as was done for Pb. Since the U.S. GEOTRACES NAZT section from which Hayes et al. (2015)'s  $K_d$  values were derived did not include hydrothermal  $p\text{Mn}$  (Lam et al., 2015a), we calculated new end-member  $K_d$  values for the entire EPZT section using the same method as Hayes et al. (2015). The calculated  $K_d$  values from the EPZT are 0.5 and 2.6 times higher than the values from the NAZT for  $\text{Fe}(\text{OH})_3$  and  $\text{MnO}_2$ , respectively (Table 1). Applying these  $K_d$  values, the  $K^{\text{MnO}_2}(\text{Pa}) = K_d^{\text{MnO}_2}(\text{Pa}) \times [p\text{MnO}_2]$  is much higher than  $K^{\text{Fe}(\text{OH})_3}(\text{Pa}) = K_d^{\text{Fe}(\text{OH})_3}(\text{Pa}) \times [p\text{Fe}(\text{OH})_3]$  at almost all stations (Fig. 11b), which does not agree with our observation of preferential scavenging by  $\text{Fe}(\text{OH})_3$  in the far-field (Fig. 12b, d). Since our  $p\text{Mn}$  speciation results suggest that freshly-formed hydrothermal  $p\text{Mn}$  may have different mineralogy and scavenging affinity than the  $p\text{Mn}$  in the rest of the section, another set of end-member  $K_d$  values was calculated using the near-field and far-field plumes data from 2000 to 3000 m depth range exclusively. The low number of data points leads to high uncertainty in the derived end-member  $K_d$  values, but we can nonetheless examine the relative changes in their values. The  $K_d^{\text{MnO}_2}(\text{Pa})$  and  $K_d^{\text{Fe}(\text{OH})_3}(\text{Pa})$  derived from the near-field plume data only are similar to the values derived from the entire section data (Table 1), indicating that the near-field  $p\text{Mn}$  and  $p\text{Fe}$  largely determines the  $K_d^{\text{MnO}_2}(\text{Pa})$  and  $K_d^{\text{Fe}(\text{OH})_3}(\text{Pa})$  of the section because the concentrations of  $p\text{Mn}$  and  $p\text{Fe}$  in the near-field plume are significantly higher than in the rest of the section. These  $K_d$  values are remarkably different from those derived from the far-field plume data. The  $K_d^{\text{MnO}_2}(\text{Pa})$  and  $K_d^{\text{Fe}(\text{OH})_3}(\text{Pa})$  derived from the far-field plume data are two orders of magnitude lower and an order of magnitude higher, respectively, than their near-field  $K_d$  values (Table 1). If we calculate  $K^{\text{MnO}_2}(\text{Pa})$  and  $K^{\text{Fe}(\text{OH})_3}(\text{Pa})$  for the near-field and far-field plumes using the corresponding  $K_d$  values, the result shows that  $^{231}\text{Pa}$  is preferentially adsorbed to  $\text{MnO}_2$  in the near-field plume but to  $\text{Fe}(\text{OH})_3$  in the far-field plume (Fig. 11c), which is consistent with what is observed in the tracer-tracer plots. Although the  $K_d$  values used for this study have large uncertainties originating from the small number of data used in the calculation, the result suggests that freshly-formed  $\text{MnO}_2$  in the near-field plume has higher

Table 1

End-member partition coefficients of  $^{231}\text{Pa}$  ( $K_d(\text{Pa})$ ) for  $\text{Fe}(\text{OH})_3$  and  $\text{MnO}_2$  derived from various sets of data. The method used to compute these numbers is written in detail in Hayes et al. (2015). The EPZT plume data are from 2000 to 3000 m depth range.

Data used	$K_d^{\text{Fe}(\text{OH})_3}(\text{Pa})(\text{g}/\text{g})$	$K_d^{\text{MnO}_2}(\text{Pa})(\text{g}/\text{g})$
NAZT: entire section	$(29.3 \pm 5.5) \times 10^6$	$(213.1 \pm 42.8) \times 10^6$
EPZT: entire section ( $n = 334$ )	$(42.7 \pm 6.2) \times 10^6$	$(765.9 \pm 69.4) \times 10^6$
EPZT: near-field plume ( $n = 22$ )	$(26.0 \pm 39.6) \times 10^6$	$(699.3 \pm 308.2) \times 10^6$
EPZT: far-field plume ( $n = 50$ )	$(204.7 \pm 65.0) \times 10^6$	$(8.2 \pm 1646.5) \times 10^6$

affinity for  $^{231}\text{Pa}$  than the aged pMn in the far-field plume. The highly-reactive Mn oxides quickly grow and settle out in the near-field plume, and Mn oxides with lower reactivity may be advected to the far-field plume. As discussed in Section 4.3.2, the decrease in scavenging affinity in the far-field plume may be related to the mineralogy of pMn in the far-field plume being different from that of the near-field pMn. For  $\text{Fe}(\text{OH})_3$ , far-field plume particles appear to have higher sorption capacity than the near-field ones. The pFe in the near-field hydrothermal plume is mainly nanoparticulate  $\text{Fe}(\text{III})$ oxyhydrates (100–200 nm in diameter) collocated with organic matter, but at station 21, the pFe transforms to more discrete minerals embedded within an organic matrix (Fitzsimmons et al., 2017; Hoffman et al., 2018). Such morphological transition may be related to the increase in the scavenging affinity of  $\text{Fe}(\text{OH})_3$ . Further investigation on the chemistry and mechanism of  $^{231}\text{Pa}$  adsorption to metal oxides will help in understanding the processes occurring in the hydrothermal plume.

## 5. CONCLUSION

In this study, we have explored the cycling of particulate Mn in the hydrothermal plume from the 15°S EPR using synchrotron X-ray microscopy and spectroscopy techniques. Direct observations of the oxidation state and mineralogy of Mn in marine particles are scarce due to their low Mn concentrations. Dick et al. (2009) reported on some mineralogical characteristics of Mn oxides collected in the vicinity of the hydrothermal vent, but this is the first study reporting changes of Mn oxidation state in hydrothermal particles during the dispersal of a plume.

In the near-field plume within ~80 km of the ridge axis, oxidized Mn composed primarily of  $\delta\text{-MnO}_2$  and triclinic birnessite was found in both SSF and LSF particles. In this plume, microbially-mediated Mn oxidation precipitates Mn (IV)-rich  $\delta\text{-MnO}_2$ , which is followed by autocatalytic oxidation of dMn(II) that ripens  $\delta\text{-MnO}_2$  to triclinic birnessite and deposits more Mn(III/IV) oxides. These reactions continuously occur while pMn grows and aggregates with other pFe and organic particles, resulting in large aggregates that are enriched in Mn relative to the other elements. These large aggregates rapidly settle out during transport and are not found in the far-field plume. We hypothesize that these fresh biogenic Mn oxides are also particularly reactive to scavenging trace elements such as Co, Mo, and  $^{231}\text{Pa}$ , and these elements are also removed by sinking of Mn oxides in the near-field.

In the far-field plume, oxidized Mn was found in the SSF particles. Because additional Mn oxidation does not occur in the far-field (Resing et al., 2015), we speculate that a small portion of the near-field SSF pMn that was not subject to autocatalysis and aggregation was advected to the far-field plume. This pMn may have ripened to Mn(IV)-bearing minerals that are different from the near-field Mn oxides because their Mn(III) fractions are smaller than the near-field SSF pMn. These particles are less reactive to scavenging given that no correlation is observed between pMn and pCo, pMo, and p $^{231}\text{Pa}$  in the far-field plume. The far-field LSF pMn was dominated by reduced Mn as a

result of Mn oxides removal in the near-field and slow aggregation of small, oxidized pMn to large particles in the far-field plume.

The results of this study highlight the importance of autocatalytic Mn oxidation as well as microbially-mediated oxidation in Mn oxides formation in the near-field plume. The study also reveals that the scavenging of other elements by Mn oxides may be confined to the near-field plume where fresh Mn oxides are present, implying that hydrothermal pMn in the distal plume may be less significant for the deep-sea removal of trace elements despite its long-range transport. Although this study is focused on Mn oxides in a single hydrothermal plume, the principles may apply elsewhere in the water column. For instance, microbially-mediated Mn oxides are known to be formed in the upper ocean (Cowen and Bruland, 1985; Sunda and Huntsman, 1988; Moffett, 1997) except in the euphotic layers where Mn oxides are photoreduced (Sunda et al., 1983; Sunda and Huntsman, 1988). Freshly-formed biogenic Mn oxides in the upper water column would be analogous to the Mn oxides in the near-field plume with high adsorption capacities. On the other hand, aged Mn oxides that settle to deeper water may have ripened to different Mn minerals like far-field plume particles and thus have reduced reactivity. Our hypothesis is supported by Hawco et al. (2018) where they showed that Co scavenging by Mn oxides mostly occurs in the upper water (<1500 m), and deep-sea Co scavenging is very slow. The Mn-Co correlation is observed in all waters below the euphotic layer, however, because of the settling of the Co-carrying Mn oxides from the upper water column (Hawco et al., 2018). This is not the case in a hydrothermal plume that is horizontally spreading because settling of the Mn-Co oxides removes the particles from the plume. The detailed changes occurring in Mn oxides during settling in the water column may differ from those occurring in the hydrothermal plume, and further investigation is required to understand the changes in the mineralogy of Mn oxides during aging and their effect on adsorption chemistry.

## Declaration of Competing Interest

The authors declare that they have no known competing financial interests or personal relationships that could have appeared to influence the work reported in this paper.

## ACKNOWLEDGEMENT

We would like to thank Dan Ohnemus, Erin Black, Sarah Nicholas and S. Pike for operating in-situ pumps and processing particle samples on board during the GP16 cruise. The authors also thank Sirine Fakra and Sharon Bone for their support at the ALS and SSRL facilities and Martin Fleisher for operating the LDEO ICP-MS facility. Portions of this research were carried out at the Advanced Light Source, a U.S. DOE Office of Science User Facility under contract no. DE-AC02-05CH11231, and at the Stanford Synchrotron Radiation Lightsource, supported by the U.S. Department of Energy, Office of Science, Office of Basic Energy Sciences under Contract No. DE-AC02-76SF00515. The SSRL Structural Molecular Biology Program is supported by the DOE Office of Biological and Environmental Research, and by the

National Institutes of Health, National Institute of General Medical Sciences (P30GM133894). The contents of this publication are solely the responsibility of the authors and do not necessarily represent the official views of NIGMS or NIH. This research was supported by the Chemical Oceanography program through the National Science Foundation under grant number NSF OCE-1518110 to P.J.L., NSF OCE-1233688 to R.F.A. and M.Q.F., and NSF OCE-1233903 to R.L.E. and H.C. The particulate trace elements (pTE) and  $^{231}\text{Pa}$  ( $p^{231}\text{Pa}$ ) concentrations data from the U.S. GEOTRACES EPZT cruise can be found at the Biological and Chemical Oceanography Data Management Office (BCO-DMO): <https://www.bco-dmo.org/dataset/668083> for pTE and <http://www.bco-dmo.org/dataset/676231> for  $p^{231}\text{Pa}$ .

## APPENDIX A. SUPPLEMENTARY MATERIAL

Supplementary data to this article can be found online at <https://doi.org/10.1016/j.gca.2021.02.020>.

## REFERENCES

- Adams D. K., McGillicuddy D. J., Zamudio L., Thurnherr A. M., Liang X. F., Rouxel O., German C. R. and Mullineaux L. S. (2011) Surface-generated mesoscale eddies transport deep-sea products from hydrothermal vents. *Science* **332**, 580–583.
- Allredge A. L. and Cohen Y. (1987) Can microscale chemical patches persist in the sea – Microelectrode study of marine snow, fecal pellets. *Science* **235**, 689–691.
- Bam W., Maiti K., Baskaran M., Krupp K., Lam P. J. and Xiang Y. (2020) Variability in Pb-210 and Po-210 partition coefficients (K-d) along the US GEOTRACES Arctic transect. *Mar. Chem.* **219**.
- Bargar J. R., Brown G. E. and Parks G. A. (1997) Surface complexation of Pb(II) at oxide-water interfaces.2. XAFS and bond-valence determination of mononuclear Pb(II) sorption products and surface functional groups on iron oxides. *Geochim. Cosmochim. Acta* **61**, 2639–2652.
- Bargar J. R., Tebo B. M., Bergmann U., Webb S. M., Glatzel P., Chiu V. Q. and Villalobos M. (2005a) Biotic and abiotic products of Mn(II) oxidation by spores of the marine *Bacillus* sp. strain SG-1. *Am. Mineral.* **90**, 143–154.
- Bargar J. R., Tebo B. M. and Villinski J. E. (2000) In situ characterization of Mn(II) oxidation by spores of the marine *Bacillus* sp strain SG-1. *Geochim. Cosmochim. Acta* **64**, 2775–2778.
- Bargar J. R., Webb S. M. and Tebo B. M. (2005b) EXAFS, XANES and in-situ SR-XRD characterization of biogenic manganese oxides produced in sea water. *Phys. Scripta* **T115**, 888–890.
- Barling J. and Anbar A. D. (2004) Molybdenum isotope fractionation during adsorption by manganese oxides. *Earth Planet Sci. Lett.* **217**, 315–329.
- Bennett S. A., Statham P. J., Green D. R. H., Le Bris N., McDermott J. M., Prado F., Rouxel O. J., Von Damm K. and German C. R. (2011) Dissolved and particulate organic carbon in hydrothermal plumes from the East Pacific Rise, 9 degrees 50 ' N. *Deep-Sea Res. Pt. I* **58**, 922–931.
- Bennett S. A., Van Dover C., Breier J. A. and Coleman M. (2015) Effect of depth and vent fluid composition on the carbon sources at two neighboring deep-sea hydrothermal vent fields (Mid-Cayman Rise). *Deep-Sea Res. Pt. I* **104**, 122–133.
- Bianchi D., Weber T. S., Kiko R. and Deutsch C. (2018) Global niche of marine anaerobic metabolisms expanded by particle microenvironments. *Nat. Geosci.* **11**, 263–268.
- Bishop J. K. B., Lam P. J. and Wood T. J. (2012) Getting good particles: Accurate sampling of particles by large volume in-situ filtration. *Limnol. Oceanogr. Methods* **10**, 681–710.
- Bostrom K. and Peterson M. N. (1966) Precipitates from hydrothermal exhalations on East Pacific Rise. *Econ. Geol.* **61**, 1258–1265.
- Bostrom K. and Peterson M. N. (1969) Origin of aluminum-poor ferromanganous sediments in areas of high heat flow on East Pacific Rise. *Mar. Geol.* **7**, 427–447.
- Boyle E. A., Zurbrick C., Lee J. M., Till R., Till C. P., Zhang J. and Flegal A. R. (2020) Lead and lead isotopes in the U.S. GEOTRACES East Pacific Zonal Transect (GEOTRACES GP16). *Mar. Chem.* <https://doi.org/10.1016/j.marchem.2020.103892>.
- Breier J. A., Toner B. M., Fakra S. C., Marcus M. A., White S. N., Thurnherr A. M. and German C. R. (2012) Sulfur, sulfides, oxides and organic matter aggregated in submarine hydrothermal plumes at 9 degrees 50'N East Pacific Rise. *Geochim. Cosmochim. Acta* **88**, 216–236.
- Butterfield C. N., Soldatova A. V., Lee S. W., Spiro T. G. and Tebo B. M. (2013) Mn(II, III) oxidation and MnO<sub>2</sub> mineralization by an expressed bacterial multicopper oxidase. *Proc. Natl. Acad. Sci. U.S.A.* **110**, 11731–11735.
- Campbell A. C., Gieskes J. M., Lupton J. E. and Lonsdale P. F. (1988) Manganese geochemistry in the Guaymas Basin, Gulf of California. *Geochim. Cosmochim. Acta* **52**, 345–357.
- Cowen J. P. (1992) Morphological-study of marine bacterial capsules – Implications for marine aggregates. *Mar. Biol.* **114**, 85–95.
- Cowen J. P., Bertram M. A., Baker E. T., Feely R. A., Massoth G. J. and Summit M. (1998) Geomicrobial transformation of manganese in Gorda Ridge event plumes. *Deep-Sea Res. Pt. II* **45**, 2713–2737.
- Cowen J. P. and Bruland K. W. (1985) Metal deposits associated with bacteria – Implications for Fe and Mn Marine Biogeochemistry. *Deep-Sea Res.* **32**, 253–272.
- Cowen J. P. and Li Y. H. (1991) The influence of a changing bacterial community on trace-metal scavenging in a deep-sea particle plume. *J. Mar. Res.* **49**, 517–542.
- Cowen J. P., Massoth G. J. and Baker E. T. (1986) Bacterial scavenging of Mn and Fe in a mid-field to far-field hydrothermal particle plume. *Nature* **322**, 169–171.
- Cowen J. P., Massoth G. J. and Feely R. A. (1990) Scavenging rates of dissolved manganese in a hydrothermal vent plume. *Deep-Sea Res.* **37**, 1619–1637.
- Crowther D. L., Dillard J. G. and Murray J. W. (1983) The mechanism of Co(II) oxidation on synthetic birnessite. *Geochim. Cosmochim. Acta* **47**, 1399–1403.
- Cutter G. and Bruland K. W. (2012) Rapid and noncontaminating sampling system for trace elements in global ocean surveys. *Limnol. Oceanogr. Methods.* <https://doi.org/10.4319/lom.2012.10.425>.
- Davies S. H. R. and Morgan J. J. (1989) Manganese(II) oxidation-kinetics on metal-oxide surfaces. *J. Colloid Interf. Sci.* **129**, 63–77.
- Dick G. J., Clement B. G., Webb S. M., Fodrie F. J., Bargar J. R. and Tebo B. M. (2009) Enzymatic microbial Mn(II) oxidation and Mn biooxide production in the Guaymas Basin deep-sea hydrothermal plume. *Geochim. Cosmochim. Acta* **73**, 6517–6530.
- Dick G. J., Lee Y. E. and Tebo B. M. (2006) Manganese(II)-oxidizing bacillus spores in Guaymas Basin hydrothermal sediments and plumes. *Appl. Environ. Microb.* **72**, 3184–3190.
- Dick G. J., Torpey J. W., Beveridge T. J. and Tebo B. A. (2008) Direct identification of a bacterial Manganese(II) oxidase, the multicopper oxidase MnxG, from spores of several different

- marine *Bacillus* species. *Appl. Environ. Microb.* **74**, 1527–1534.
- Dymond J. and Roth S. (1988) Plume dispersed hydrothermal particles – A time-series record of settling flux from the endeavor ridge using moored sensors. *Geochim. Cosmochim. Acta* **52**, 2525–2536.
- Edmond J. M., Vondamm K. L., McDuff R. E. and Measures C. I. (1982) Chemistry of hot springs on the East Pacific Rise and their effluent dispersal. *Nature* **297**, 187–191.
- Ehrlich H. L. (1983) Manganese-oxidizing bacteria from a hydrothermally active area on the galapagos rift. *Ecol. Bull.*, 357–366.
- Feely R. A., Baker E. T., Marumo K., Urabe T., Ishibashi J., Gendron J., Lebon G. T. and Okamura K. (1996) Hydrothermal plume particles and dissolved phosphate over the superfast-spreading southern East Pacific Rise. *Geochim. Cosmochim. Acta* **60**, 2297–2323.
- Feng X. H., Zhu M. Q., Ginder-Vogel M., Ni C. Y., Parikh S. J. and Sparks D. L. (2010) Formation of nano-crystalline todorokite from biogenic Mn oxides. *Geochim. Cosmochim. Acta* **74**, 3232–3245.
- Field M. P. and Sherrell R. M. (2000) Dissolved and particulate Fe in a hydrothermal plume at 9 degrees 45'N, East Pacific Rise: Slow Fe (II) oxidation kinetics in Pacific plumes. *Geochim. Cosmochim. Acta* **64**, 619–628.
- Fitzsimmons J. N., John S. G., Marsay C. M., Hoffman C. L., Nicholas S. L., Toner B. M., German C. R. and Sherrell R. M. (2017) Iron persistence in a distal hydrothermal plume supported by dissolved-particulate exchange. *Nat. Geosci.* **10**, 195–201.
- Francis C. A. and Tebo B. M. (2002) Enzymatic Manganese(II) oxidation by metabolically dormant spores of diverse *Bacillus* species. *Appl. Environ. Microb.* **68**, 874–880.
- German C. R., Campbell A. C. and Edmond J. M. (1991) Hydrothermal scavenging at the Mid-Atlantic Ridge – Modification of trace-element dissolved fluxes. *Earth Planet Sci. Lett.* **107**, 101–114.
- German C. R., Klinkhammer G. P., Edmond J. M., Mitra A. and Elderfield H. (1990) Hydrothermal scavenging of rare-earth elements in the ocean. *Nature* **345**, 516–518.
- German C. R. and Seyfried, Jr., W. E. (2014) Hydrothermal processes. In *Treatise on Geochemistry* (eds. H. D. Holland and K. K. Turekian). Elsevier, pp. 191–233.
- Hansel C. M. and Learman D. R. (2015) Geomicrobiology of manganese. In *Ehrlich's Geomicrobiology* (eds. H. L. Ehrlich, D. K. Newman and A. Kappler), sixth ed. CRC Press, pp. 401–452.
- Hansel C. M., Zeiner C. A., Santelli C. M. and Webb S. M. (2012) Mn(II) oxidation by an ascomycete fungus is linked to superoxide production during asexual reproduction. *Proc. Natl. Acad. Sci. U.S.A.* **109**, 12621–12625.
- Hautala S. L. and Riser S. C. (1993) A nonconservative beta-spiral determination of the deep circulation in the Eastern South-Pacific. *J. Phys. Oceanogr.* **23**, 1975–2000.
- Hawco N. J., Lam P. J., Lee J. M., Ohnemus D. C., Noble A. E., Wyatt N. J., Lohan M. C. and Saito M. A. (2018) Cobalt scavenging in the mesopelagic ocean and its influence on global mass balance: Synthesizing water column and sedimentary fluxes. *Mar. Chem.* **201**, 151–166.
- Hawco N. J., Ohnemus D. C., Resing J. A., Twining B. S. and Saito M. A. (2016) A dissolved cobalt plume in the oxygen minimum zone of the eastern tropical South Pacific. *Biogeochemistry* **13**, 5697–5717.
- Hayes C. T., Anderson R. F., Fleisher M. Q., Vivancos S. M., Lam P. J., Ohnemus D. C., Huang K. F., Robinson L. F., Lu Y. B., Cheng H., Edwards R. L. and Moran S. B. (2015) Intensity of Th and Pa scavenging partitioned by particle chemistry in the North Atlantic Ocean. *Mar. Chem.* **170**, 49–60.
- Heller M. I., Lam P. J., Moffett J. W., Till C. P., Lee J. M., Toner B. M. and Marcus M. A. (2017) Accumulation of Fe oxyhydroxides in the Peruvian oxygen deficient zone implies non-oxygen dependent Fe oxidation. *Geochim. Cosmochim. Acta* **211**, 174–193.
- Ho P., Lee J. M., Heller M. I., Lam P. J. and Shiller A. M. (2018) The distribution of dissolved and particulate Mo and V along the US GEOTRACES East Pacific Zonal Transect (GP16): The roles of oxides and biogenic particles in their distributions in the oxygen deficient zone and the hydrothermal plume. *Mar. Chem.* **201**, 242–255.
- Hoffman C. L., Nicholas S. L., Ohnemus D. C., Fitzsimmons J. N., Sherrell R. M., German C. R., Heller M. I., Lee J. M., Lam P. J. and Toner B. M. (2018) Near-field iron and carbon chemistry of non-buoyant hydrothermal plume particles, Southern East Pacific Rise 15 degrees S. *Mar. Chem.* **201**, 183–197.
- Jenkins W. J., Lott D. E., German C. R., Cahill K. L., Goudreau J. and Longworth B. (2018) The deep distributions of helium isotopes, radiocarbon, and noble gases along the US GEOTRACES East Pacific Zonal Transect (GP16). *Mar. Chem.* **201**, 167–182.
- Jiang H. S. and Breier J. A. (2014) Physical controls on mixing and transport within rising submarine hydrothermal plumes: A numerical simulation study. *Deep-Sea Res. Pt. I* **92**, 41–55.
- Johnson J. E., Savalia P., Davis R., Kocar B. D., Webb S. M., Nealson K. H. and Fischer W. W. (2016) Real-time manganese phase dynamics during biological and abiotic manganese oxide reduction. *Environ. Sci. Technol.* **50**, 4248–4258.
- Johnson J. E., Webb S. M., Thomas K., Ono S., Kirschvink J. L. and Fischer W. W. (2013) Manganese-oxidizing photosynthesis before the rise of cyanobacteria. *Proc. Natl. Acad. Sci. U.S.A.* **110**, 11238–11243.
- Junta J. and Hochella M. F. (1994) Manganese(II) oxidation at mineral surfaces – A microscopic and spectroscopic study. *Geochim. Cosmochim. Acta* **58**, 4985–4999.
- Jurgensen A., Widmeyer J. R., Gordon R. A., Bendell-Young L. I., Moore M. M. and Crozier E. D. (2004) The structure of the manganese oxide on the sheath of the bacterium *Leptothrix discophora*: An XAFS study. *Am. Mineral.* **89**, 1110–1118.
- Kashiwabara T., Takahashi Y., Tanimizu M. and Usui A. (2011) Molecular-scale mechanisms of distribution and isotopic fractionation of molybdenum between seawater and ferromanganese oxides. *Geochim. Cosmochim. Acta* **75**, 5762–5784.
- Klawonn I., Bonaglia S., Bruchert V. and Ploug H. (2015) Aerobic and anaerobic nitrogen transformation processes in N-2-fixing cyanobacterial aggregates. *ISME J.* **9**, 1456–1466.
- Klinkhammer G. and Hudson A. (1986) Dispersal patterns for hydrothermal plumes in the South-Pacific using manganese as a tracer. *Earth Planet Sci. Lett.* **79**, 241–249.
- Klinkhammer G. P. (1980) Observations of the distribution of manganese over the East Pacific Rise. *Chem. Geol.* **29**, 211–226.
- Lam P. J., Bishop J. K. B., Henning C. C., Marcus M. A., Waychunas G. A. and Fung I. Y. (2006) Wintertime phytoplankton bloom in the subarctic Pacific supported by continental margin iron. *Global Biogeochem. Cycl.* **20**. <https://doi.org/10.1029/2005GB002557>.
- Lam P. J., Lee J. M., Heller M. I., Mehic S., Xiang Y. and Bates N. R. (2018) Size-fractionated distributions of suspended particle concentration and major phase composition from the US GEOTRACES Eastern Pacific Zonal Transect (GP16). *Mar. Chem.* **201**, 90–107.
- Lam P. J., Ohnemus D. C. and Auro M. E. (2015a) Size-fractionated major particle composition and concentrations

- from the US GEOTRACES North Atlantic Zonal Transect. *Deep-Sea Res. Pt. II* **116**, 303–320.
- Lam P. J., Twining B. S., Jeandel C., Roychoudhury A., Resing J. A., Santschi P. H. and Anderson R. F. (2015b) Methods for analyzing the concentration and speciation of major and trace elements in marine particles. *Prog. Oceanogr.* **133**, 32–42.
- Lamborg C. H., Hammerschmidt C. R. and Bowman K. L. (2016) An examination of the role of particles in oceanic mercury cycling. *Philos. T. R. Soc. A* **374**. <https://doi.org/10.1098/rsta.2015.0297>.
- Landrot G., Ginder-Vogel M., Livi K., Fitts J. P. and Sparks D. L. (2012) Chromium(III) oxidation by three poorly crystalline Manganese(IV) oxides. 1. Chromium(III)-oxidizing capacity. *Environ. Sci. Technol.* **46**, 11594–11600.
- Lanson B., Drits V. A., Feng Q. and Manceau A. (2002) Structure of synthetic Na-birnessite: Evidence for a triclinic one-layer unit cell. *Am. Mineral.* **87**, 1662–1671.
- Learman D. R., Voelker B. M., Vazquez-Rodriguez A. I. and Hansel C. M. (2011a) Formation of manganese oxides by bacterially generated superoxide. *Nat. Geosci.* **4**, 95–98.
- Learman D. R., Wankel S. D., Webb S. M., Martinez N., Madden A. S. and Hansel C. M. (2011b) Coupled biotic-abiotic Mn(II) oxidation pathway mediates the formation and structural evolution of biogenic Mn oxides. *Geochim. Cosmochim. Acta* **75**, 6048–6063.
- Lee J. M., Heller M. I. and Lam P. J. (2018) Size distribution of particulate trace elements in the US GEOTRACES Eastern Pacific Zonal Transect (GP16). *Mar. Chem.* **201**, 108–123.
- Lee Y. and Tebo B. M. (1994) Cobalt(II) oxidation by the marine Manganese(II)-oxidizing *Bacillus* Sp strain Sg-1. *Appl. Environ. Microb.* **60**, 2949–2957.
- Ling F. T., Post J. E., Heaney P. J. and Ilton E. S. (2018) The relationship between Mn oxidation state and structure in triclinic and hexagonal birnessites. *Chem. Geol.* **479**, 216–227.
- Lupton J. E. and Craig H. (1981) A major He-3 source at 15-degrees-S on the East Pacific Rise. *Science* **214**, 13–18.
- Luther G. W. (2005) Manganese(II) oxidation and Mn(IV) reduction in the environment – Two one-electron transfer steps versus a single two-electron step. *Geomicrobiol. J.* **22**, 195–203.
- Luther G. W. (2010) The role of one- and two-electron transfer reactions in forming thermodynamically unstable intermediates as barriers in multi-electron redox reactions. *Aquat. Geochem.* **16**, 395–420.
- Manceau A., Lanson M. and Takahashi Y. (2014) Mineralogy and crystal chemistry of Mn, Fe Co, Ni, and Cu in a deep-sea Pacific polymetallic nodule. *Am. Mineral.* **99**, 2068–2083.
- Manceau A., Marcus M. A. and Grangeon S. (2012) Determination of Mn valence states in mixed-valent manganates by XANES spectroscopy. *Am. Mineral.* **97**, 816–827.
- Mandernack K. W., Post J. and Tebo B. M. (1995) Manganese mineral formation by bacterial-spores of the marine bacillus, strain Sg-1 – Evidence for the direct oxidation of Mn(II) to Mn (IV). *Geochim. Cosmochim. Acta* **59**, 4393–4408.
- Mandernack K. W. and Tebo B. M. (1993) Manganese scavenging and oxidation at hydrothermal vents and in vent plumes. *Geochim. Cosmochim. Acta* **57**, 3907–3923.
- Martin P. A. and Lea D. W. (2002) A simple evaluation of cleaning procedures on fossil benthic foraminiferal Mg/Ca. *Geochem. Geophys. Geosyst.* **3**. <https://doi.org/10.1029/2001GC000280>.
- Mckenzie R. M. (1980) Adsorption of lead and other heavy-metals on oxides of manganese and iron. *Aust. J. Soil Res.* **18**, 61–73.
- Miyata N., Tani Y., Iwahori K. and Soma M. (2004) Enzymatic formation of manganese oxides by an Acremonium-like hyphomycete fungus, strain KR21-2. *FEMS Microbiol. Ecol.* **47**, 101–109.
- Moffett J. W. (1997) The importance of microbial Mn oxidation in the upper ocean: a comparison of the Sargasso Sea and equatorial Pacific. *Deep-Sea Res. Pt. I* **44**, 1277–1291.
- Moffett, J.W., Cutter, G.A., German, C.R., Gegg, S.R., 2014. “GTC bottle data along the US GEOTRACES East Pacific Zonal Transect from the R/V Thomas G. Thompson TN303 cruise in the tropical Pacific from Peru to Tahiti during 2013 (U.S. GEOTRACES EPZT project)”. Biological and Chemical Oceanography Data Management Office (BCO-DMO) Dataset version 10/30/2014. <https://www.bco-dmo.org/dataset/503133>.
- Moffett J. W. and Ho J. (1996) Oxidation of cobalt and manganese in seawater via a common microbially catalyzed pathway. *Geochim. Cosmochim. Acta* **60**, 3415–3424.
- Murray K. J., Webb S. M., Bargar J. R. and Tebo B. M. (2007) Indirect oxidation of Co(II) in the presence of the marine Mn (II)-oxidizing bacterium *Bacillus* sp strain SG-1. *Appl. Environ. Microb.* **73**, 6905–6909.
- Nealson K. H. and Ford J. (1980) Surface enhancement of bacterial manganese oxidation – Implications for aquatic environments. *Geomicrobiol. J.* **2**, 21–37.
- Nealson K. H., Tebo B. M. and Rosson R. A. (1988) Occurrence and mechanisms of microbial oxidation of manganese. *Adv. Appl. Microbiol.* **33**, 279–318.
- Nelson Y. M., Lion L. W., Ghiorse W. C. and Shuler M. L. (1999a) Production of biogenic Mn oxides by *Leprothrix discophora* SS-1 in a chemically defined growth medium and evaluation of their Pb adsorption characteristics. *Appl. Environ. Microb.* **65**, 175–180.
- Nelson Y. M., Lion L. W., Shuler M. L. and Ghiorse W. C. (1999b) Lead binding to metal oxide and organic phases of natural aquatic biofilms. *Limnol. Oceanogr.* **44**, 1715–1729.
- Newville M. (2001) IFEFFIT: interactive XAFS analysis and FEFF fitting. *J. Synchrotron. Rad.* **8**, 322–324.
- Nicholas S. L., Erickson M. L., Woodruff L. G., Knaeble A. R., Marcus M. A., Lynch J. K. and Toner B. M. (2017) Solid-phase arsenic speciation in aquifer sediments: A micro-X-ray absorption spectroscopy approach for quantifying trace-level speciation. *Geochim. Cosmochim. Acta* **211**, 228–255.
- Nico P. S. and Zasoski R. J. (2000) Importance of Mn(III) availability on the rate of Cr(III) oxidation on delta-MnO<sub>2</sub>. *Environ. Sci. Technol.* **34**, 3363–3367.
- Niedermiller J. and Baskaran M. (2019) Comparison of the scavenging intensity, remineralization and residence time of Po-210 and Pb-210 at key zones (biotic, sediment-water and hydrothermal) along the East Pacific GEOTRACES transect. *J. Environ. Radioact.* **198**, 165–188.
- Pavia F., Anderson R., Vivancos S., Fleisher M., Lam P., Lu Y. B., Cheng H., Zhang P. and Edwards R. L. (2018) Intense hydrothermal scavenging of Th-230 and Pa-231 in the deep Southeast Pacific. *Mar. Chem.* **201**, 212–228.
- Peers G. and Price N. M. (2004) A role for manganese in superoxide dismutases and growth of iron-deficient diatoms. *Limnol. Oceanogr.* **49**, 1774–1783.
- Ploug H., Kuhl M., Buchholz-Cleven B. and Jorgensen B. B. (1997) Anoxic aggregates – An ephemeral phenomenon in the pelagic environment? *Aquat. Microb. Ecol.* **13**, 285–294.
- Postma D. (1985) Concentration of Mn and separation from Fe in sediments-I. Kinetics and stoichiometry of the reaction between birnessite and dissolved Fe(II) at 10°C. *Geochim. Cosmochim. Acta* **49**, 1023–1033.
- Postma D. and Appelo C. A. J. (2000) Reduction of Mn-oxides by ferrous iron in a flow system: Column experiment and reactive transport modelling. *Geochim. Cosmochim. Acta* **64**, 1237–1247.
- Raven J. A. (1990) Predictions of Mn and Fe use efficiencies of phototrophic growth as a function of light availability for growth and of C assimilation pathway. *New Phytol.* **116**, 1–18.

- Resing J. A., Sedwick P. N., German C. R., Jenkins W. J., Moffett J. W., Sohst B. M. and Tagliabue A. (2015) Basin-scale transport of hydrothermal dissolved metals across the South Pacific Ocean. *Nature* **523**, 200–U140.
- Rudnicki M. D. and Elderfield H. (1993) A chemical-model of the buoyant and neutrally buoyant plume above the Tag Vent Field, 26 Degrees-N, Mid-Atlantic Ridge. *Geochim. Cosmochim. Acta* **57**, 2939–2957.
- Schwertmann U. and Cornell R. M. (2000) *Iron Oxides in the Laboratory: Preparation and Characterization*. Wiley.
- Shimmield G. B. and Price N. B. (1988) The scavenging of U, Th-230 and Pa-231 during pulsed hydrothermal activity at 20-degrees-S, East Pacific Rise. *Geochim. Cosmochim. Acta* **52**, 669–677.
- Silvester E., Manceau A. and Drits V. A. (1997) Structure of synthetic monoclinic Na-rich birnessite and hexagonal birnessite: II. Results from chemical studies and EXAFS spectroscopy. *Am. Mineral.* **82**, 962–978.
- Sunda W. G. and Huntsman S. A. (1988) Effect of sunlight on redox cycles of manganese in the Southwestern Sargasso Sea. *Deep-Sea Res.* **35**, 1297–1317.
- Sunda W. G., Huntsman S. A. and Harvey G. R. (1983) Photo-reduction of manganese oxides in seawater and its geochemical and biological implications. *Nature* **301**, 234–236.
- Talley L. D. and Johnson G. C. (1994) Deep, zonal subequatorial currents. *Science* **263**, 1125–1128.
- Tanaka K., Yu Q. Q., Sasaki K. and Ohnuki T. (2013) Cobalt(II) oxidation by biogenic Mn oxide produced by *Pseudomonas* sp strain NGY-1. *Geomicrobiol. J.* **30**, 874–885.
- Tanaka M., Ariga D., Kashiwabara T. and Takahashi Y. (2018) Adsorption mechanism of Molybdenum(VI) on manganese oxides causing a large isotope fractionation. *ACS Earth Space Chem.* **2**, 1187–1195.
- Tang Y., Stewart G., Lam P. J., Rigaud S. and Church T. (2017) The influence of particle concentration and composition on the fractionation of Po-210 and Pb-210 along the North Atlantic GEOTRACES transect GA03. *Deep-Sea Res. Pt. I* **128**, 42–54.
- Tang Y. Z., Zeiner C. A., Santelli C. M. and Hansel C. M. (2013) Fungal oxidative dissolution of the Mn(II)-bearing mineral rhodochrosite and the role of metabolites in manganese oxide formation. *Environ. Microbiol.* **15**, 1063–1077.
- Tebo B. M. (1991) Manganese(II) oxidation in the suboxic zone of the Black-Sea. *Deep-Sea Res.* **38**, S883–S905.
- Tebo B. M., Bargar J. R., Clement B. G., Dick G. J., Murray K. J., Parker D., Verity R. and Webb S. M. (2004) Biogenic manganese oxides: Properties and mechanisms of formation. *Annu. Rev. Earth Pl. Sci.* **32**, 287–328.
- Thamdrup B., Glud R. N. and Hansen J. W. (1994) Manganese oxidation and in-situ manganese fluxes from a coastal sediment. *Geochim. Cosmochim. Acta* **58**, 2563–2570.
- Van Cappellen P., Viollier E., Roychoudhury A., Clark L., Ingall E., Lowe K. and Dichristina T. (1998) Biogeochemical cycles of manganese and iron at the oxic-anoxic transition of a stratified marine basin (Orca Basin, Gulf of Mexico). *Environ. Sci. Technol.* **32**, 2931–2939.
- vanWaasbergen L. G., Hildebrand M. and Tebo B. M. (1996) Identification and characterization of a gene cluster involved in manganese oxidation by spores of the marine *Bacillus* sp strain SG-1. *J. Bacteriol.* **178**, 3517–3530.
- Villalobos M., Bargar J. and Sposito G. (2005) Mechanisms of Pb (II) sorption on a biogenic manganese oxide. *Environ. Sci. Technol.* **39**, 569–576.
- Villalobos M., Toner B., Bargar J. and Sposito G. (2003) Characterization of the manganese oxide produced by *Pseudomonas putida* strain MnB1. *Geochim. Cosmochim. Acta* **67**, 2649–2662.
- von Damm K. L. (1990) Seafloor hydrothermal activity – Black smoker chemistry and chimneys. *Annu. Rev. Earth Pl. Sci.* **18**, 173–204.
- Wasylenki L. E., Rolfe B. A., Weeks C. L., Spiro T. G. and Anbar A. D. (2008) Experimental investigation of the effects of temperature and ionic strength on Mo isotope fractionation during adsorption to manganese oxides. *Geochim. Cosmochim. Acta* **72**, 5997–6005.
- Webb S. M. (2005) SIXpack: a graphical user interface for XAS analysis using IFEFFIT. *Phys. Scripta* **T115**, 1011–1014.
- Webb S. M. (2011) The microanalysis toolkit: X-ray fluorescence image processing software. *AIP Conf. Proc.*, 196–199.
- Webb S. M., Tebo B. M. and Bargar J. R. (2005a) Structural influences of sodium and calcium ions on the biogenic manganese oxides produced by the marine *Bacillus* sp., strain SG-1. *Geomicrobiol. J.* **22**, 181–193.
- Webb S. M., Tebo B. M. and Bargar J. R. (2005b) Structural characterization of biogenic Mn oxides produced in seawater by the marine bacillus sp strain SG-1. *Am. Mineral.* **90**, 1342–1357.
- Wilson A. R., Lion L. W., Nelson Y. M., Shuler M. L. and Ghiorse W. C. (2001) The effects of pH and surface composition of Pb adsorption to natural freshwater biofilms. *Environ. Sci. Technol.* **35**, 3182–3189.
- Xiang Y. and Lam P. J. (2020) Size-fractionated compositions of marine suspended particles in the Western Arctic Ocean: lateral and vertical sources. *J. Geophys. Res.: Oceans* **n/a**. <https://doi.org/10.1029/2020JC016144>, e2020JC016144.
- Yang P., Post J. E., Wang Q., Xu W. Q., Geiss R., McCurdy P. R. and Zhu M. Q. (2019) Metal adsorption controls stability of layered manganese oxides. *Environ. Sci. Technol.* **53**, 7453–7462.
- Zhao W., Cui H. J., Liu F., Tan W. F. and Feng X. H. (2009) Relationship between Pb<sup>2+</sup> adsorption and average Mn oxidation state in synthetic birnessites. *Clay Clay Miner.* **57**, 513–520.

Associate editor: Colleen M. Hansel